

Ion Crystal Metamorphoses in a Paul trap

V. Ursekar, J. M. Silvester, Y. S. Nam, and R. Blümel

Department of Physics, Wesleyan University,

Middletown, Connecticut 06459-0155, USA

(Dated: December 9, 2021)

Abstract

The standard second-order pseudo-oscillator potential used in many analytical investigations of the properties of ions stored in a Paul trap has serious limitations. In this paper we show that ion-crystal configurations exhibited by 2, 3, and 4 simultaneously stored ions in a Paul trap are not predicted by the standard pseudo-oscillator potential, but are all captured qualitatively and quantitatively by an extended pseudopotential derived in this paper. The power of our extended pseudopotential extends in particular to the prediction of the border lines between different crystal configurations (morphologies) in the Paul trap's a, q stability diagram. In the three- and four-ion cases, several of the ion-crystal structures predicted by our improved pseudopotential have never been observed experimentally before. We present them here as a challenge for experiments.

PACS numbers: 37.10.Ty, 52.27.Jt, 52.50.Qt

I. INTRODUCTION

Periodically driven systems abound in atomic, molecular, and optical (AMO) physics. Examples are laser interactions with atoms and ions [1, 2], Rydberg atoms in strong external microwave fields [3–6], excitation of molecular rotation by periodic microwave pulses [7], and charged particles in electrodynamic traps [8–10]. Treating the radiation field classically, all these periodically driven AMO systems are governed by a time-periodic Hamiltonian

$$\hat{H}(t+T) = \hat{H}(t), \quad (1)$$

where T is the period of the driving field. The wavefunction of the system then satisfies the periodically driven Schrödinger equation

$$i\hbar \frac{\partial |\psi(t)\rangle}{\partial t} = \hat{H}(t) |\psi(t)\rangle, \quad (2)$$

where \hbar is Planck's constant. This equation may be solved formally by the linear, unitary time evolution operator

$$\hat{U}(t') |\psi(t)\rangle = |\psi(t'+t)\rangle. \quad (3)$$

Because of the linearity of (2), the time-evolution operator \hat{U} satisfies the operator identity

$$\hat{U}(t') \hat{U}(t) = \hat{U}(t'+t). \quad (4)$$

Since $\hat{U}(t)$ is unitary for all t , $\hat{U}(T)$ is unitary and may be written as

$$\hat{U}(T) = \exp\left(\frac{i}{\hbar} \hat{W}T\right), \quad (5)$$

where \hat{W} is a Hermitian operator, also known as the *quasi-energy* operator [11]. With the help of \hat{W} we define the propagator

$$\hat{P}(t) = \exp\left(\frac{i}{\hbar} \hat{W}t\right), \quad (6)$$

which interpolates smoothly between the values of $\hat{U}(NT)$, N integer, and agrees with $\hat{U}(t)$ at integer multiples of the driving period T . The quasi-energy operator \hat{W} , with its associated propagator $\hat{P}(t)$, is all we need to obtain a stroboscopic description of the time evolution of the wavefunction at multiples of the driving period T :

$$|\psi(NT)\rangle = \hat{U}(NT) |\psi(0)\rangle = \exp\left(\frac{i}{\hbar} \hat{W}NT\right) |\psi(0)\rangle = \hat{P}(NT) |\psi(0)\rangle. \quad (7)$$

We may use the operator \hat{W} to obtain a smoothed time evolution of $|\psi\rangle$ on the macro-scale T according to

$$|\psi(t)\rangle \approx |\varphi(t)\rangle = \hat{P}(t)|\psi(0)\rangle, \quad (8)$$

where, in line with our stroboscopic picture, the smoothed motion described by $|\varphi(t)\rangle$ agrees with the exact time evolution of $|\psi(t)\rangle$ at multiples of the drive-period T according to

$$|\varphi(NT)\rangle = |\psi(NT)\rangle. \quad (9)$$

Because $|\varphi(t)\rangle$ describes the motion on the macro-scale T , we call the motion represented by $\hat{P}(t)$ and its associated wavefunction $|\varphi(t)\rangle$ the *macromotion*. In order to obtain the exact time evolution, but keeping the convenient description provided by $|\varphi(t)\rangle$ on the macro-scale, we define the reduced propagator

$$\hat{Q}(t) = \exp\left[-\frac{i}{\hbar}\hat{W}(t \bmod T)\right] \hat{U}(t \bmod T), \quad (10)$$

which is defined on the time interval $[0, T]$. With the help of \hat{W} and $\hat{Q}(t)$, the complete time-evolution operator $\hat{U}(t)$ may now be factored exactly into two parts,

$$\hat{U}(t) = \hat{P}(t)\hat{Q}(t), \quad (11)$$

where the first factor, $\hat{P}(t)$, describes the macromotion and the second factor, $\hat{Q}(t)$, describes the motion on the fine scale between multiples of T . Therefore, we call the motion described by $\hat{Q}(t)$ the *micromotion*. Defining $t = NT + \tau$, where $0 \leq \tau < T$, it can be shown immediately that (11) is indeed exact: Because of the definition of τ , we have $\tau = t \bmod T$, and therefore

$$\begin{aligned} \hat{P}(t)\hat{Q}(t) &= \exp\left(\frac{i}{\hbar}\hat{W}(NT + \tau)\right) \exp\left(-\frac{i}{\hbar}\hat{W}\tau\right) \hat{U}(\tau) \\ &= \exp\left(\frac{i}{\hbar}\hat{W}NT\right) \hat{U}(\tau) \\ &= \hat{U}(NT)\hat{U}(\tau) = \hat{U}(NT + \tau) = \hat{U}(t), \end{aligned} \quad (12)$$

where we used the operator identity (4). The separation into a slow macromotion, described by the quasi-energy operator \hat{W} and its associated propagator \hat{P} , and a fast micromotion, described by the propagator \hat{Q} , is extremely useful in all cases in which we are more interested in the large-scale time evolution of a driven system than in its precise, in most

cases extremely high-frequency behavior between driving periods. Therefore, looking at the system on the coarse-grained time scale T , governed by the interpolating time-evolution operator \hat{P} , we have succeeded in transforming an *explicitly time-dependent* system, described by the Hamiltonian $\hat{H}(t)$, containing time-periodic drive terms, into a *time-independent* system, described by the new quasi-energy Hamiltonian \hat{W} . The analogy between \hat{W} and a conventional time-independent Hamiltonian is further strengthened by the observation that in many cases, at least to lowest order, \hat{W} may be written as the sum of a kinetic-energy operator \hat{K} and a potential-energy operator, called the *pseudopotential*, or, in the AMO context, the ponderomotive potential [12].

Formally, and in a physics context on the quantum level, this separation expresses the mathematical content of *Floquet's Theorem* [13, 14], a 19th century theorem, first derived in connection with periodically driven linear systems of equations.

The usefulness of the separation (11) of the time-evolution operator into slow macro-motion and fast micromotion components cannot be overstated. It is the basis of much of quantum chaos research [15] with its implications for AMO physics [16, 17], where the focus is on the spectral properties of \hat{W} [18].

For many driven AMO systems, in particular for strong driving fields and large quantum numbers, a classical description of the driven atomic system makes sense [3–6]. Motivated by the corresponding quantum systems, we are led to the question: Is an exact quasi-energy description also possible for these classical AMO systems? At first glance, the answer seems to be “no”, since these classical systems are, in general, non-linear, while Floquet's Theorem, and all the procedures discussed above, are applicable only for linear (quantum) systems. However, contrary to expectations, a classical separation into a macromotion part and a micromotion part is indeed possible. In particular, it is possible to construct a classical pseudopotential [19] that averages over the fast, classical time scales and results in an effective pseudo-Hamiltonian that is the classical analog of \hat{W} . However, these procedures are not exact. While, as shown above, it is straightforward on the quantum level to exactly and explicitly separate the time-evolution operator into a slow, macro-motion component, and a fast, micro-motion component, a similar, generally valid decomposition, in analogy to the quantum procedures, is not known on the classical level. Usually, in particular in connection with ion-trapping systems [8–10], the first-order pseudopotential, as constructed in [19], is used. This, however, as shown in [20–22], may not capture qualitatively important features

even on the slow, macro-scale. Therefore, using the trapping of up to four ions in a Paul trap as our example, the purpose of this paper is to outline a generalizable procedure that is capable of constructing higher-order pseudopotentials to better approximate the time-independent Paul-trap pseudo-Hamiltonian. We will show that our improved pseudopotential is capable of predicting crystalline structures (morphologies) of ions in the Paul trap that are completely beyond the predictive power of the simple, lowest-order pseudopotential constructed according to [19]. We consider the discovery of these unconventional three- and four-ion morphologies not only as an illustration of the predictive power of our improved pseudopotentials, but also as a challenge for experimentalists to confirm the existence of these exotic structures in the lab.

Our paper is structured as follows. In Sec. II we introduce the time-dependent equations of motion of ions simultaneously stored in a Paul trap. These equations of motion are the basis and starting point of all of our work described in this paper. In this section we also give a brief introduction into the pseudopotential method, illustrated for the case of two simultaneously stored ions. In Sec. III A, we develop a general mathematical procedure that may be applied to a system of charged particles stored in the Paul trap. In Sec. III B, and going beyond the 2-ion case discussed in [20–22], we apply the formalism developed in Sec. III A to the specific case of three stored ions to obtain an improved pseudopotential for this case. In Sec. IV we revisit the case of two particles in the Paul trap to highlight the power of the improved pseudopotential, as this is the simplest possible case in the presence of an interparticle potential. In particular, we will show how the improved pseudopotential reveals new physics, beyond what is predicted by the standard pseudopotential. Then, in Sec. V, together with the pseudopotential expression derived in Sec. III, and the demonstrated method of revealing new physics in Sec. IV, we investigate the three-particle case in detail, where we report morphology boundary lines of different ion-crystal configurations in the Paul trap. In Sec. VI we present numerical results on the four-particle case and address how our general formalism may be applied. In Sec. VII we discuss our results and in Sec. VIII we summarize and conclude our paper.

II. TIME-DEPENDENT EQUATIONS OF MOTION

As shown in Fig. 1, a Paul trap [8–10] consists of a concentric arrangement of three conducting surfaces, a hyperbolic ring electrode and two electrically connected hyperbolic end-cap electrodes. As described in the literature [8–10], applying a combination of ac and dc voltages between the ring- and end-cap electrodes produces a time-dependent quadrupole potential capable of storing N ions simultaneously for very long periods of time. Storage times ranging from hours [23] to days [24] with up to 10^5 simultaneously stored ions [23] have been reported.

In this paper, we treat the stored ions in the classical approximation. Even if the ions are in their crystalline state [10, 25, 26], this approximation is expected to be excellent due to the large distances between ions in conventional traps (of the order of μm [10, 25, 26]) and their relatively large temperatures (no effort is usually made to cool ion crystals to their quantum ground state, although this has been demonstrated [27] to be possible in the single-ion case).

Measuring time in units of

$$t_0 = \frac{2}{\omega}, \quad (13)$$

where ω is the angular frequency of the driving ac voltage, and distances in units of

$$l_0 = \left(\frac{Q^2}{\pi\epsilon_0 m \omega^2} \right)^{1/3}, \quad (14)$$

where Q is the charge of the stored particles, m is their mass, and ϵ_0 is the permittivity of the vacuum, the classical equations of motion in an ideal Paul trap [8, 9] are given by

$$\ddot{\vec{R}}_i + \gamma \dot{\vec{R}}_i + [a + 2q \cos(2\tau)] \begin{pmatrix} X_i \\ Y_i \\ -2Z_i \end{pmatrix} = \sum_{\substack{j=1 \\ j \neq i}}^N \frac{\vec{R}_i - \vec{R}_j}{|\vec{R}_i - \vec{R}_j|^3}, \quad i = 1, \dots, N, \quad (15)$$

where $\vec{R}_i = (X_i, Y_i, Z_i)$ is the position vector of ion number i in units of l_0 , γ is a damping constant, τ is the time in units of t_0 , and a, q , given by

$$a = \frac{8QV_{\text{dc}}}{m\omega^2(r_0^2 + 2z_0^2)}, \quad q = \frac{4QV_{\text{ac}}}{m\omega^2(r_0^2 + 2z_0^2)}, \quad (16)$$

are the dimensionless control parameters of the trap, proportional to the applied dc and ac voltages, V_{dc} and V_{ac} , respectively, and r_0 and z_0 in (16) are the distances of the ring electrode and the end-cap electrodes from the center of the trap, respectively.

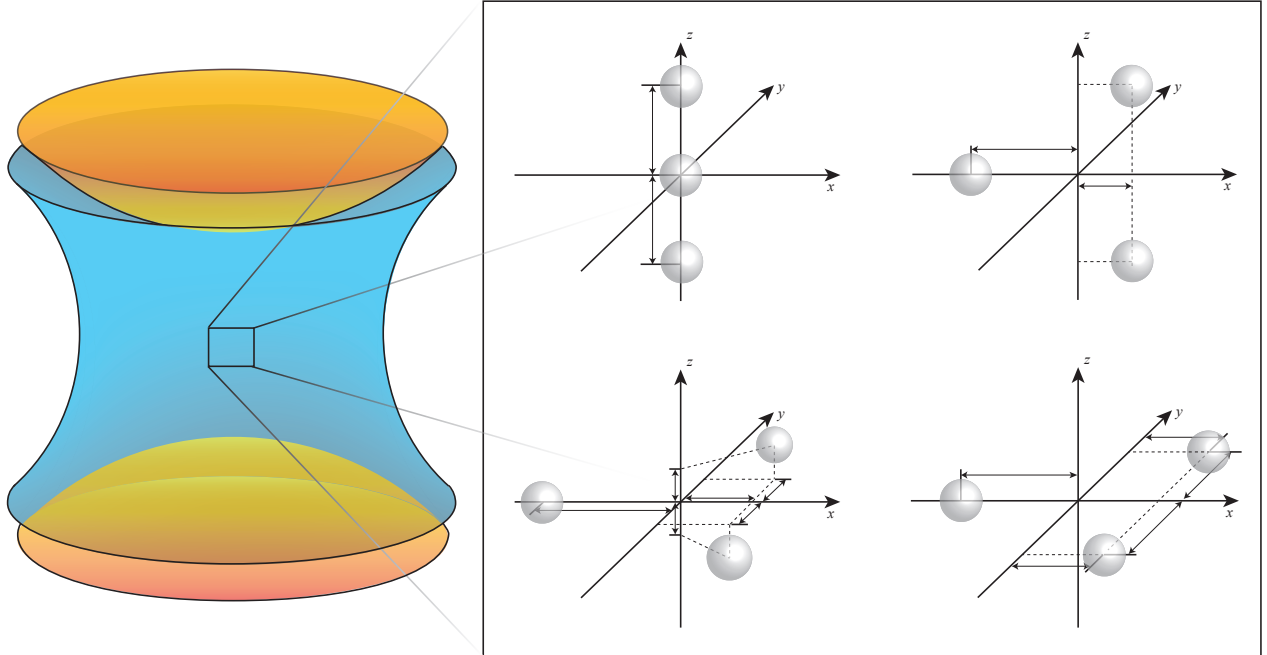


FIG. 1: (Color Online) Electrode configuration of a Paul trap (left) together with four possible orientations of a three-particle Coulomb crystal in a Paul trap (box on the right). The Paul trap consists of two end-cap electrodes (orange) at top and bottom and a ring electrode (blue), both of which are connected to ac and dc voltage sources (not shown). Shown to the right, inside the box, are the observed three-particle crystal configurations in a Paul trap, obtained from numerical simulations. The four configurations are rod (top-left), pop-out (top-right), tilt (bottom-left), and planar (bottom-right), where, as indicated by their positions, illustrated by arrows and dashed lines, the center of mass of each of the configurations is located at the origin, i.e., the center of the Paul trap.

The damping constant γ in (15) deserves a few comments. It may be used two ways. (i) Frequently in the literature [10], this constant is used to simulate actual ion cooling present in ion-trapping experiments. (ii) Our use of this damping constant is different. We are

interested in the properties of ion crystals in the ideal Paul trap in the absence of damping. Therefore, in all of our simulations, we use γ only as an auxiliary device to cool ion clouds [10, 28] into crystals. Once the crystals have formed, we slowly switch off γ so that we may assess ion-crystal properties for $\gamma = 0$. It is known that ion crystals, once in the crystalline state, and even though they are driven by the trap's ac field, do not show any energy gain [10, 29]. Therefore, in the absence of external heat sources, and even for $\gamma = 0$, they remain in their crystal state forever. In the following, wherever in this paper we refer to simulations of the equations of motion (15), we imply that the γ -switch-off method just described is used to produce ion crystals in our ideal Paul trap. Since $\gamma = 0$ at the end of our ion-crystal formation process, and since ion crystals are stable in the absence of γ , none of the crystal properties reported in this paper, as it should be, depend on γ .

The set of equations of motion (15) is the basis of our work described in this paper. Whenever we need to compare the predictions of our analytical approximations to the predictions of the exact dynamics, we use numerical solutions of the equations of motion (15), obtained by integrating (15) with the help of standard 4th- and 5th-order Runge-Kutta differential-equation solvers [30].

A first analytical stab at the equations of motion (15) was done long ago using the method of averaging [19] to derive a time-averaged, time-independent pseudopotential, the standard pseudopotential

$$U_{eff}^{(s)} = \frac{1}{2} \sum_{i=1}^N [\mu_x^2 X_i^2 + \mu_y^2 Y_i^2 + \mu_z^2 Z_i^2] + \frac{1}{2} \sum_{\substack{i,j=1 \\ j \neq i}}^N \frac{1}{|\vec{R}_i - \vec{R}_j|}, \quad (17)$$

in which the N ions are confined, despite their repulsive Coulomb interactions, subjected to the standard pseudo-oscillator with oscillator frequencies [29]

$$\mu_x = \mu_y = \left(a + \frac{1}{2} q^2 \right)^{1/2}, \quad \mu_z = [2(q^2 - a)]^{1/2}. \quad (18)$$

In some regions of the (q, a) control-parameter space, this potential is excellent and describes crystal configurations very well. In other parts of the (q, a) control-parameter space the standard pseudopotential (17) fails completely, even missing, as we will see, most of the possible crystal morphologies predicted by (15). For the three-ion case this is illustrated in the box of Fig. 1, which shows the four possible morphologies of a three-ion crystal, predicted by (15), of which one of them (the tilted crystal) is completely missed by the

standard pseudopotential (17) (for more details see below). The inadequacy of the standard pseudopotential in this respect was first pointed out in [20–22] for the two-ion case, and an adequate, improved pseudopotential, capable of describing all two-ion morphologies, was derived in [20, 22]. It is the purpose of this paper to improve the standard pseudopotential (17) such that it is powerful enough to predict, in addition to the two-ion case, all crystal morphologies and transition boundaries between them in (q, a) control-parameter space for three and four simultaneously stored particles. We will see that the exact equations of motion (15) predict a rich menagerie of exotic three- and four-particle crystal morphologies that are all captured by our improved pseudopotentials derived in the following sections. Our methods are generalizable and, in addition to the Paul trap, applicable to many other periodically driven AMO systems.

III. THREE-PARTICLE PSEUDOPOTENTIAL

Since the improved pseudopotential for the two-ion case is already known [20, 22], we focus in this section on the derivation of the improved three-particle pseudopotential. Following this section, the formal machinery will be in place to apply our results to the two-ion case (Sec. IV), the three-ion case (Sec. V), and the four-ion case (Sec. VI).

A. Derivation of a generalized pseudopotential in a driven system

We start with the following set of three coupled differential equations

$$\begin{aligned}
 m_X \ddot{X} &= -U_X(X, Y, Z) - k_X X \cos(\omega t), \\
 m_Y \ddot{Y} &= -U_Y(X, Y, Z) - k_Y Y \cos(\omega t), \\
 m_Z \ddot{Z} &= -U_Z(X, Y, Z) - k_Z Z \cos(\omega t),
 \end{aligned}
 \tag{19}$$

where m_I , $I \in \{X, Y, Z\}$, denote effective masses, $U_I = \partial U / \partial I$, and k_I are constants. The system (19) is generic and describes a variety of dynamical systems, of which one is the Paul trap. The treatment of a general, n -coordinate system is available in Appendix A. Here, we investigate the case $n = 3$, which will be of particular importance in connection with the three-particle morphology to be discussed in detail in Sec. III B.

Following [19], assuming that the $\cos(\omega t)$ terms in (19) oscillate fast compared to the motion governed by U , we may write

$$\begin{aligned} X(t) &= x(t) + \xi \cos(\omega t), \\ Y(t) &= y(t) + \eta \cos(\omega t), \\ Z(t) &= z(t) + \zeta \cos(\omega t), \end{aligned} \tag{20}$$

where x, y, z denote the slowly varying macromotion coordinates and ξ, η, ζ denote the amplitudes of the rapidly oscillating micromotion in their respective directions. The micromotion amplitudes are assumed to vary slowly over the time scale of the macromotion and hence may be assumed to be constant over a cycle of the driving field. Assuming now that the micromotion amplitudes are small, we may expand $U(X, Y, Z)$ in the micromotion amplitudes up to second order according to

$$\begin{aligned} U(X, Y, Z) &\approx U(x, y, z) + U_x \xi \cos(\omega t) + U_y \eta \cos(\omega t) + U_z \zeta \cos(\omega t) \\ &\quad + \frac{1}{2} U_{xx} \xi^2 \cos^2(\omega t) + \frac{1}{2} U_{yy} \eta^2 \cos^2(\omega t) + \frac{1}{2} U_{zz} \zeta^2 \cos^2(\omega t) \\ &\quad + U_{xy} \xi \eta \cos^2(\omega t) + U_{yz} \eta \zeta \cos^2(\omega t) + U_{zx} \zeta \xi \cos^2(\omega t), \end{aligned} \tag{21}$$

where, for $i, j \in \{x, y, z\}$ ($I, J \in \{X, Y, Z\}$), U_i or U_{ij} denote, in their respective order, $\partial U / \partial I$ or $\partial^2 U / \partial I \partial J$, evaluated at $X = x, Y = y$, and $Z = z$. The first derivative of (21) in X , evaluated at (x, y, z) , then reads

$$\begin{aligned} U_X &\approx U_x + U_{xx} \xi \cos(\omega t) + U_{yx} \eta \cos(\omega t) + U_{zx} \zeta \cos(\omega t) \\ &\quad + \frac{1}{2} U_{xxx} \xi^2 \cos^2(\omega t) + \frac{1}{2} U_{yyx} \eta^2 \cos^2(\omega t) + \frac{1}{2} U_{zzx} \zeta^2 \cos^2(\omega t) \\ &\quad + U_{xyx} \xi \eta \cos^2(\omega t) + U_{yzx} \eta \zeta \cos^2(\omega t) + U_{zxx} \zeta \xi \cos^2(\omega t) \end{aligned} \tag{22}$$

and similar expressions may be obtained straightforwardly for Y and Z . Together with (20), inserting (22) and its corresponding Y and Z parts into (19) and equating like powers of $\cos(\omega t)$, we obtain

$$\begin{aligned} m_X \omega^2 \xi &= U_{xx} \xi + U_{yx} \eta + U_{zx} \zeta + k_X x, \\ m_Y \omega^2 \eta &= U_{yy} \eta + U_{zy} \zeta + U_{xy} \xi + k_Y y, \\ m_Z \omega^2 \zeta &= U_{zz} \zeta + U_{xz} \xi + U_{yz} \eta + k_Z z. \end{aligned} \tag{23}$$

Solving for the micromotion amplitudes, we obtain

$$\begin{aligned}
\xi &= \{k_X x[(m_Y \omega^2 - U_{yy})(m_Z \omega^2 - U_{zz}) - U_{yz}^2] \\
&\quad + k_Y y[U_{yx}(m_Z \omega^2 - U_{zz}) + U_{xz}U_{yz}] \\
&\quad + k_Z z[U_{zx}(m_Y \omega^2 - U_{yy}) + U_{xy}U_{zy}]\}/\Delta, \\
\eta &= \{k_Y y[(m_Z \omega^2 - U_{zz})(m_X \omega^2 - U_{xx}) - U_{zx}^2] \\
&\quad + k_Z z[U_{zy}(m_X \omega^2 - U_{xx}) + U_{yx}U_{zx}] \\
&\quad + k_X x[U_{xy}(m_Z \omega^2 - U_{zz}) + U_{yz}U_{xz}]\}/\Delta, \\
\zeta &= \{k_Z z[(m_X \omega^2 - U_{xx})(m_Y \omega^2 - U_{yy}) - U_{xy}^2] \\
&\quad + k_X x[U_{xz}(m_Y \omega^2 - U_{yy}) + U_{zy}U_{xy}] \\
&\quad + k_Y y[U_{yz}(m_X \omega^2 - U_{xx}) + U_{zx}U_{yx}]\}/\Delta,
\end{aligned} \tag{24}$$

where

$$\begin{aligned}
\Delta &= (m_X \omega^2 - U_{xx})(m_Y \omega^2 - U_{yy})(m_Z \omega^2 - U_{zz}) \\
&\quad - (m_X \omega^2 - U_{xx})U_{yz}^2 - (m_Y \omega^2 - U_{yy})U_{zx}^2 \\
&\quad - (m_Z \omega^2 - U_{zz})U_{xy}^2 - 2U_{xy}U_{yz}U_{zx}.
\end{aligned} \tag{25}$$

This time, together with (20) and (22), averaging (19) over one cycle of the driving field, results in

$$\begin{aligned}
m_X \ddot{x} &= -U_x - \frac{1}{4}U_{xxx}\xi^2 - \frac{1}{4}U_{yyx}\eta^2 - \frac{1}{4}U_{zzx}\zeta^2 \\
&\quad - \frac{1}{2}U_{xyx}\xi\eta - \frac{1}{2}U_{yzx}\eta\zeta - \frac{1}{2}U_{zxx}\zeta\xi - \frac{1}{2}k_X\xi, \\
m_Y \ddot{y} &= -U_y - \frac{1}{4}U_{xxy}\xi^2 - \frac{1}{4}U_{yyy}\eta^2 - \frac{1}{4}U_{zzy}\zeta^2 \\
&\quad - \frac{1}{2}U_{xyy}\xi\eta - \frac{1}{2}U_{yzy}\eta\zeta - \frac{1}{2}U_{zxy}\zeta\xi - \frac{1}{2}k_Y\eta, \\
m_Z \ddot{z} &= -U_z - \frac{1}{4}U_{xxz}\xi^2 - \frac{1}{4}U_{yyz}\eta^2 - \frac{1}{4}U_{zzz}\zeta^2 \\
&\quad - \frac{1}{2}U_{xyz}\xi\eta - \frac{1}{2}U_{yzz}\eta\zeta - \frac{1}{2}U_{zxz}\zeta\xi - \frac{1}{2}k_Z\zeta.
\end{aligned} \tag{26}$$

This set of equations of motion may be derived from the potential

$$U_{\text{eff}}(x, y, z) = U(x, y, z) + \frac{1}{4}k_X x\xi + \frac{1}{4}k_Y y\eta + \frac{1}{4}k_Z z\zeta, \tag{27}$$

which may be verified by direct differentiation.

B. Application of the generalized pseudopotential to the Paul-trap dynamics

Having presented the general analytical framework, in this subsection we now apply our results to the special case of three particles in the Paul trap. In particular, we are interested in investigating crystalline structures formed in the Paul trap.

Any N -particle ion crystal, in particular the three-ion crystal we focus on in this section, is characterized by the geometric order in which the particles assemble themselves [10, 24, 29, 31], and, in addition, by the fact that this order is maintained during a micromotion cycle, during which the ions of a crystal execute a breathing motion around their equilibrium positions. Thus, due to this strong geometric correlation, knowing the coordinates (X, Y, Z) of a *single* ion of the crystal, supplemented with the geometric configuration of the crystal, allows us to know the coordinates of all the other ions in the crystal. Fundamentally, therefore, the N -ion crystal problem is reduced to a single-particle problem. In the case of the three-ion crystal, the focus of this section, we choose the coordinates of the topmost ion (see box in Fig. 1) to characterize the entire crystal. As shown in Fig. 2, we denote its coordinates by (X, Y, Z) . Knowing (X, Y, Z) , together with the condition that the center of mass of this crystal is located at the center of the trap, is enough to know all coordinates (X_i, Y_i, Z_i) , $i = 1, 2, 3$, of the three-ion crystal.

Having chosen our coordinates, we now derive equations of motion for three particles in a Paul trap. We start with the Lagrangian of the system

$$\mathcal{L} = [T^{(1)} + T^{(2)} + T^{(3)}] - [U_{\text{Trap}}^{(1)} + U_{\text{Trap}}^{(2)} + U_{\text{Trap}}^{(3)}] - [U_{\text{Coul}}^{(1)-(2)} + U_{\text{Coul}}^{(2)-(3)} + U_{\text{Coul}}^{(3)-(1)}], \quad (28)$$

where, for (X_i, Y_i, Z_i) and $(\dot{X}_i, \dot{Y}_i, \dot{Z}_i)$, the positions and velocities of the i th particle, respectively, in suitable dimensionless units [32],

$$T^{(i)} = \frac{1}{2}(\dot{X}_i^2 + \dot{Y}_i^2 + \dot{Z}_i^2) \quad (29)$$

denotes the kinetic energy of the i th particle,

$$U_{\text{Trap}}^{(i)} = U_{\text{Trap}}(X_i, Y_i, Z_i) = \frac{1}{2}[a + 2q \cos(2\tau)](X_i^2 + Y_i^2 - 2Z_i^2) \quad (30)$$

denotes the trap potential of the i th particle, and

$$U_{\text{Coul}}^{(i)-(j)} = \frac{1}{\sqrt{(X_i - X_j)^2 + (Y_i - Y_j)^2 + (Z_i - Z_j)^2}} \quad (31)$$

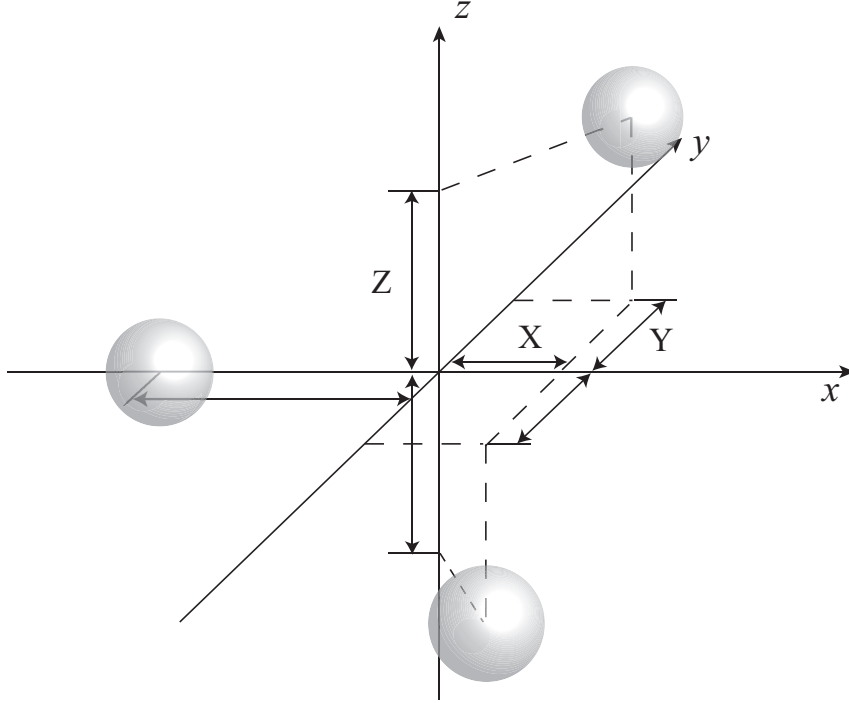


FIG. 2: Coordinate choice for the three-particle crystal formed in the Paul trap. Since the center of mass of the crystal is located at the center of the trap, knowing X, Y, Z , the coordinates of the top-most particle is enough to know the coordinates of the other two particles.

denotes the Coulomb potential between the i th and the j th particle. Using the Euler-Lagrange equations [19, 33], with (29), (30), and (31) in (28), and relating (X_i, Y_i, Z_i) to (X, Y, Z) via the center-of-mass condition, we obtain a set of three equations of motion in each of the x , y , and z directions, namely,

$$\begin{aligned}
 6\ddot{X} &= -6X[a + 2q \cos(2\tau)] + \frac{18X}{(9X^2 + Y^2 + Z^2)^{3/2}}, \\
 2\ddot{Y} &= -2Y[a + 2q \cos(2\tau)] + \frac{Y}{2(Y^2 + Z^2)^{3/2}} + \frac{2Y}{(9X^2 + Y^2 + Z^2)^{3/2}}, \\
 2\ddot{Z} &= +4Z[a + 2q \cos(2\tau)] + \frac{Z}{2(Y^2 + Z^2)^{3/2}} + \frac{2Z}{(9X^2 + Y^2 + Z^2)^{3/2}}, \quad (32)
 \end{aligned}$$

which, upon a comparison with (19), results in $m_X = 6$, $m_Y = 2$, $m_Z = 2$, $\omega = 2$, $k_X = 12q$, $k_Y = 4q$, $k_Z = -8q$, and

$$U(X, Y, Z) = \frac{2}{(9X^2 + Y^2 + Z^2)^{1/2}} + \frac{1}{2(Y^2 + Z^2)^{1/2}} + a [3X^2 + Y^2 - 2Z^2]. \quad (33)$$

We note that (X, Y, Z) in (33) may be replaced with (x, y, z) upon taking a cycle average.

Eliminating the time-dependence from (32) according to [19] to lowest order results in the pseudopotential

$$U_{\text{eff}}^{(s)} = \frac{2}{\rho} + \frac{1}{2r} + \frac{1}{2}\mu_x^2 x^2 + \frac{1}{2}\mu_y^2 y^2 + \frac{1}{2}\mu_z^2 z^2, \quad (34)$$

where $\mu_x = [6(a+q^2/2)]^{1/2}$, $\mu_y = [2(a+q^2/2)]^{1/2}$, and $\mu_z = [4(q^2-a)]^{1/2}$. The pseudopotential (34) is not capable of reproducing all four crystal morphologies shown in the box of Fig. 1 and needs to be improved. In order to obtain the improved pseudopotential (27), capable of predicting all three-ion crystal morphologies, we need the partial derivatives of U in (33). In particular,

$$\begin{aligned} U_{xx} &= 6a - \frac{18}{\rho^3} + \frac{486x^2}{\rho^5}, \\ U_{yy} &= 2a - \frac{2}{\rho^3} + \frac{6y^2}{\rho^5} - \frac{1}{2r^3} + \frac{3y^2}{2r^5}, \\ U_{zz} &= -4a - \frac{2}{\rho^3} + \frac{6z^2}{\rho^5} - \frac{1}{2r^3} + \frac{3z^2}{2r^5}, \\ U_{xy} &= \frac{54xy}{\rho^5}, \\ U_{yz} &= \frac{6yz}{\rho^5} + \frac{3yz}{2r^5}, \\ U_{zx} &= \frac{54xz}{\rho^5}, \end{aligned} \quad (35)$$

where $\rho = (9x^2 + y^2 + z^2)^{1/2}$ and $r = (y^2 + z^2)^{1/2}$, which can be used to result in

$$U_{\text{eff}} = \frac{2}{\rho} + \frac{1}{2r} + 3ax^2 + ay^2 - 2az^2 + \frac{3qx\xi\Delta + qy\eta\Delta - 2qz\zeta\Delta}{\Delta}, \quad (36)$$

where the last term on the right-hand side, while complicated, may be evaluated explicitly using (24) and (25) with the partial derivatives (35).

Our effective, generalized potential (36) allows for an improved approximation to the pseudopotential beyond the lowest-order approximation (34) via expanding (36) up to first order in $1/\text{length}$. Appendix B shows the detailed steps to arrive at the following improved

three-ion pseudopotential:

$$\begin{aligned}
\tilde{U}_{\text{eff}} = & \left[\frac{2}{\rho} + \frac{1}{2r} \right] + \left[\frac{3(2q^2 + 4a - a^2)}{4 - a} \right] x^2 + \left[\frac{2q^2 + 4a - a^2}{4 - a} \right] y^2 + \left[\frac{2(2q^2 - 2a - a^2)}{2 + a} \right] z^2 \\
& + \frac{q^2}{\rho^5} \left[\frac{324x^4}{(4 - a)^2} + \frac{4y^4}{(4 - a)^2} + \frac{4z^4}{(2 + a)^2} \right. \\
& \quad + 9x^2y^2 \left(\frac{8}{(4 - a)^2} \right) \\
& \quad - 2y^2z^2 \left(\frac{6}{(4 - a)(2 + a)} + \frac{1}{(4 - a)^2} + \frac{1}{(2 + a)^2} \right) \\
& \quad \left. - 18z^2x^2 \left(\frac{6}{(4 - a)(2 + a)} + \frac{1}{(4 - a)^2} + \frac{1}{(2 + a)^2} \right) \right] \\
& + \frac{q^2}{r^5} \left\{ \frac{y^4}{(4 - a)^2} + \frac{z^4}{(2 + a)^2} - y^2z^2 \left[\frac{1}{2(4 - a)^2} + \frac{1}{2(2 + a)^2} + \frac{3}{(4 - a)(2 + a)} \right] \right\}. \quad (37)
\end{aligned}$$

We will use this potential extensively in Sec. V.

IV. TWO-ION CRYSTAL MORPHOLOGY

Before applying the formalism developed in Sec. III to the three-ion crystals formed in the Paul trap (see Sec. V), we review, in this section, in the spirit of a template, the two-ion case studied in detail in Refs. [20, 22]. This allows us to demonstrate the power of the improved pseudopotential over the standard pseudopotential in the most straightforward manner in that the two-ion case is the simplest case that exhibits crystal morphologies not predicted by the standard pseudopotential.

We start by pointing out the fact that a crystal in a Paul trap is formed when the system is cooled, as particles find their respective, mutual, simultaneous potential minima. In terms of our improved pseudopotential this means that we may analytically determine the crystal configurations of the system by locating the minima of its pseudopotential. The potential minima may be obtained straightforwardly by setting (i) the first spatial derivatives of the potential equal to zero and (ii) requiring that the second spatial derivatives of the potential are positive. This methodology provides us with a technique that can be employed in general to investigate crystal morphologies of a system for which the governing potential is well-known, or approximately known, but sufficiently accurate. Furthermore, an additional bonus is the possibility to predict boundaries between different crystal structures, which are obtained by tracking the stability of these minima in (q, a) control-parameter space.

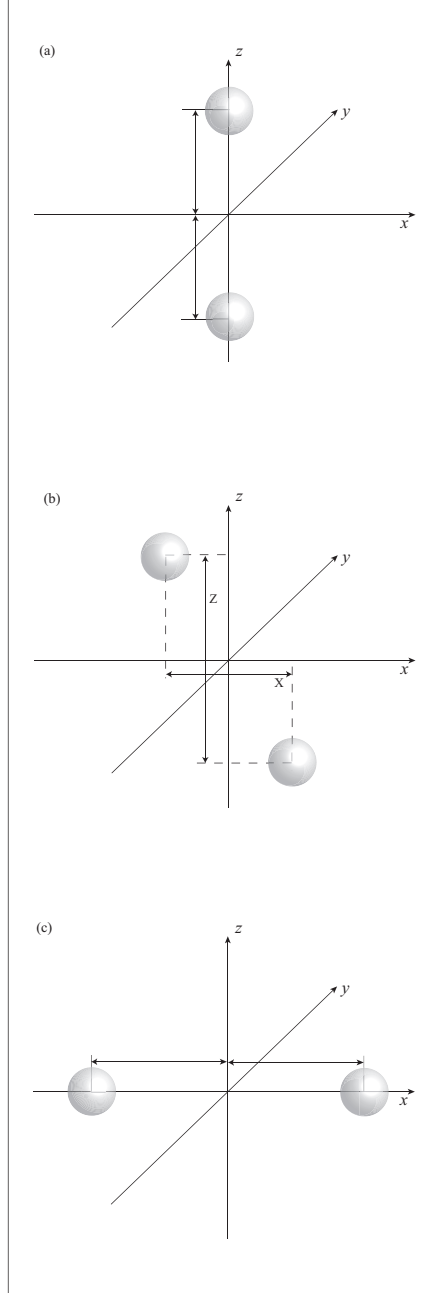


FIG. 3: Possible crystal configurations of two charged particles stored in the Paul trap. (a) shows a rod configuration, i.e., the particles are lined up along the z -axis, (b) shows a tilt configuration, i.e., the particles have non-zero polar angle with respect to the z -axis, and (c) shows a planar configuration, i.e., the particles form a horizontal rod in the x - y plane (here shown to lie along the x -axis). Motivated by the fact that the tilt orientation in (b) is the most general among all three configurations, we define the coordinates X and Z of the two-particle crystal, as shown, as the relative separation between the two ions along the x and z axes, respectively. Because of the cylindrical symmetry of the Paul trap we may, without restriction of generality, choose $Y \equiv 0$.

Applying the general pseudopotential derivation presented in Appendix A to the two-particle case, and closely following the steps presented in Sec. III B (applied to the two-particle case), we obtain the effective potential for the two-particle system according to

$$U_{\text{eff}} = \frac{1}{r_2} + \frac{1}{2}ax^2 - az^2 + \frac{qx\xi\Delta - 2qz\zeta\Delta}{\Delta}, \quad (38)$$

where

$$\begin{aligned} \xi &= [(m\omega^2 - U_{zz})k_Xx + U_{xz}k_Zz]/\Delta, \\ \zeta &= [(m\omega^2 - U_{xx})k_Zz + U_{xz}k_Xx]/\Delta, \\ \Delta &= (m\omega^2 - U_{xx})(m\omega^2 - U_{zz}) - U_{xz}^2, \end{aligned} \quad (39)$$

and

$$U_{xx} = a - \frac{1}{r_2^3} + \frac{3x^2}{r_2^5}, \quad U_{xz} = \frac{3xz}{r_2^5}, \quad U_{zz} = -2a - \frac{1}{r_2^3} + \frac{3z^2}{r_2^5}, \quad (40)$$

where $r_2 = (x^2 + z^2)^{1/2}$. Upon comparison with the two-coordinate formulation (see Appendix A), this results in $k_X = 2q$, $k_Z = -4q$, $m = 1$, $\omega = 2$. Our choice of coordinates x and z (with time averaging), along with the observed crystal orientations, is presented in Fig. 3. The potential (38) may be compared with the standard pseudopotential for the two-particle case [20, 22]

$$U_{\text{eff}}^{(s)} = \frac{1}{r_2} + \frac{1}{2} \left(a + \frac{q^2}{2} \right) x^2 + (q^2 - a)z^2. \quad (41)$$

Equipped with the two potentials (38) and (41), we are now ready to determine the potential minima by following steps (i) and (ii) as defined above to obtain the different morphology boundaries predicted by the two different pseudopotentials, thus demonstrating the power of the improved, generalized pseudopotential.

- Rod-tilt boundary. In order to extract the rod-tilt boundary, we first assume a rod-configuration, i.e., $x = 0$, and investigate the critical points of the effective potentials (38) and (41) in z . Then, we investigate the stability of the two potentials in x . A transition from a stable to an unstable potential landscape in the x -direction corresponds to a rod \leftrightarrow tilt crystal metamorphosis. The boundary of the metamorphosis satisfies the two conditions

$$\frac{1}{z} \frac{\partial U_{\text{eff}}(x=0, z)}{\partial z} = 0 \quad (42)$$

and

$$\left. \frac{\partial^2 U_{\text{eff}}(x, z)}{\partial x^2} \right|_{x=0} = 0. \quad (43)$$

Equivalent expressions hold for the standard pseudopotential $U_{\text{eff}}^{(s)}$. Numerically solving the simultaneous equations (42) and (43) [30], we obtain the two-particle rod-tilt boundary predicted by the generalized pseudopotential. The standard pseudopotential counterparts of (42) and (43) can be solved exactly and analytically, which results in the following simple analytical expression for the boundary line, i.e.,

$$a = f_{\text{rod} \leftrightarrow \text{tilt}}^{(N=2)} = \frac{1}{2}q^2. \quad (44)$$

As will be shown below, the boundary (44) predicts a degenerate case of two-particle morphologies, reflecting the inability of the standard pseudopotential to predict tilted two-ion crystals.

- Tilt-planar boundary. This time, we assume a planar configuration, i.e., $z = 0$, and investigate the critical points of the effective potentials (38) and (41) in x . Then, we investigate the stability of the potentials in z , where we look for the transition from stable to unstable configurations. The generalized pseudopotential is then subjected to the following two conditions:

$$\frac{1}{x} \frac{\partial U_{\text{eff}}(x, z=0)}{\partial x} = 0 \quad (45)$$

and

$$\left. \frac{\partial^2 U_{\text{eff}}(x, z)}{\partial z^2} \right|_{z=0} = 0. \quad (46)$$

Solving (45) and (46) results in the generalized pseudopotential prediction of the boundary line between the tilt and planar phases of two-particle crystals. Repeating the same procedure for the standard pseudopotential, which, once again, may be solved analytically, results in the boundary

$$a = f_{\text{tilt} \leftrightarrow \text{planar}}^{(N=2)} = \frac{1}{2}q^2. \quad (47)$$

The two boundaries (44) and (47) are identical. Thus, according to the standard pseudopotential, the tilt morphology is degenerate, existing only on the line $a = q^2/2$. As we will see shortly (see Fig. 4) this prediction is incorrect.

Figure 4 shows our numerical simulation results of the crystal orientations of the two-ion crystals in the Paul trap. Also shown are the boundary lines derived above [see (44) and (47) for the standard pseudopotential case]. We see that, as pointed out in [20, 22], the standard pseudopotential fails to predict the existence of the tilt-morphology, i.e., according to the standard pseudopotential this crystal phase exists only on the zero-width curve $a = q^2/2$. In fact, according to the standard pseudopotential (41), the case $a = q^2/2$ results in a radially symmetric potential, corresponding to a degenerate crystal-configuration state, where all radially symmetric morphologies (rod, tilt, and planar) are possible, but are only neutrally stable (the second derivative of the pseudopotential is zero). Thus the boundary lines predicted on the basis of the standard pseudopotential do not agree well with the exact, numerical results. In contrast, the generalized, improved pseudopotential correctly predicts the existence of all three morphologies, including the fact that they all have finite areas in (q, a) control-parameter space. In addition, for $q \lesssim 0.45$, the predicted morphology boundaries are in excellent agreement with our simulations. This is remarkable since the additional terms we keep in the generalized pseudopotential are not only improving the accuracy, but contain additional physics not contained in the lower-order standard pseudopotential. Thus, the generalized pseudopotential captures necessary, important aspects of crystal morphology observed in the Paul-trap system.

A new result, further illustrating the power of the improved pseudopotential, is the prediction of the polar angle of the tilt phase, i.e., the angle that the tilted two-ion rod crystal forms with respect to the z -axis. To this end, we approximate the generalized, improved pseudopotential in (38) up to $1/\text{length}$, following the same methodology as described in detail in Appendix B. The result is

$$\begin{aligned} \tilde{U}_{\text{eff}} = & \frac{1}{r_2} + \frac{2q^2 + 4a - a^2}{2(4 - a)}x^2 + \frac{2q^2 - 2a - a^2}{2 + a}z^2 \\ & + \frac{q^2}{r_2^5} \left[\frac{2x^4}{(4 - a)^2} + \frac{2z^4}{(2 + a)^2} - \frac{4(17 + 2a - a^2)x^2z^2}{(4 - a)^2(2 + a)^2} \right]. \end{aligned} \quad (48)$$

Assuming now that we are in the tilt phase ($x \neq 0; z \neq 0$), the polar angle is obtained as

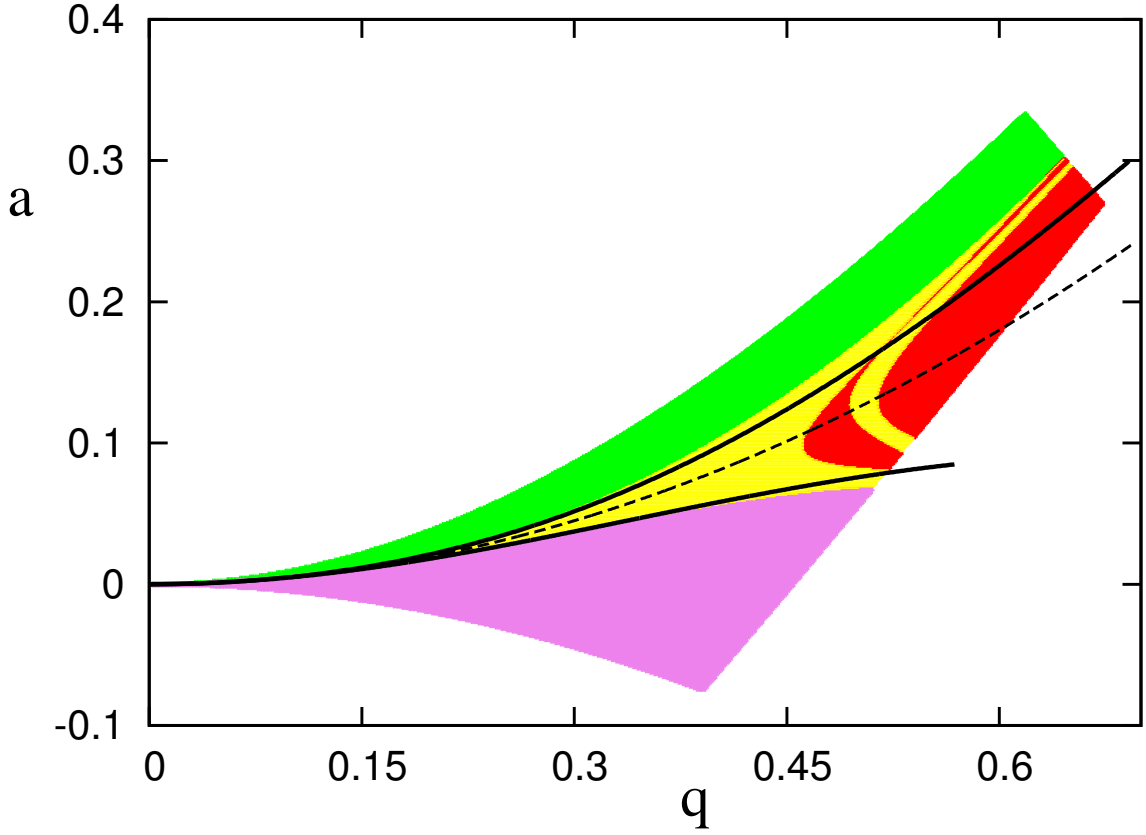


FIG. 4: (Color Online) Two-ion crystal-configuration map in (q, a) control-parameter space, obtained from numerical solutions of (15). The green region is the rod phase, yellow regions are the tilt phase, and the purple region is the planar phase. Red regions denote a non-crystal region, where the two ions are stably trapped in the Paul trap but never form a crystal [34]. The dashed line denotes the transition boundaries (44) and (47) predicted by the standard pseudopotential (41). The solid lines denote the transition boundaries predicted by the generalized pseudopotential (38). Top curve: Rod \leftrightarrow tilt boundary; bottom curve: Tilt \leftrightarrow planar boundary.

the solution of the following two simultaneous equations:

$$\begin{aligned}
\frac{1}{x} \frac{\partial \tilde{U}_{\text{eff}}}{\partial x} = & -\frac{1}{r_2^3} + \frac{2q^2 + 4a - a^2}{4 - a} \\
& - \frac{5q^2}{r_2^7} \left[\frac{2x^4}{(4 - a)^2} + \frac{2z^4}{(2 + a)^2} - \frac{4(17 + 2a - a^2)x^2z^2}{(4 - a)^2(2 + a)^2} \right] \\
& + \frac{q^2}{r_2^5} \left[\frac{8x^2}{(4 - a)^2} - \frac{8(17 + 2a - a^2)z^2}{(4 - a)^2(2 + a)^2} \right] = 0
\end{aligned} \tag{49}$$

and

$$\begin{aligned} \frac{1}{z} \frac{\partial \tilde{U}_{\text{eff}}}{\partial z} = & -\frac{1}{r_2^3} + \frac{2(2q^2 - 2a - a^2)}{2+a} \\ & - \frac{5q^2}{r_2^7} \left[\frac{2x^4}{(4-a)^2} + \frac{2z^4}{(2+a)^2} - \frac{4(17+2a-a^2)x^2z^2}{(4-a)^2(2+a)^2} \right] \\ & + \frac{q^2}{r_2^5} \left[\frac{8z^2}{(2+a)^2} - \frac{8(17+2a-a^2)x^2}{(4-a)^2(2+a)^2} \right] = 0. \end{aligned} \quad (50)$$

To obtain the solution, we subtract (50) from (49) to obtain

$$\omega_x^2 - \omega_z^2 + \frac{q^2}{r_2^3} \left\{ \frac{8 \sin^2(\theta)}{(4-a)^2} - \frac{8 \cos^2(\theta)}{(2+a)^2} - \frac{8(17+2a-a^2)}{(4-a)^2(2+a)^2} [\cos^2(\theta) - \sin^2(\theta)] \right\} = 0, \quad (51)$$

where θ is the polar angle,

$$\begin{aligned} \omega_x^2 &= \frac{2q^2 + 4a - a^2}{4-a}, \\ \omega_z^2 &= \frac{2(2q^2 - 2a - a^2)}{2+a}, \end{aligned} \quad (52)$$

$x = r_2 \sin(\theta)$, and $z = r_2 \cos(\theta)$. Adding (49) and (50) yields

$$\begin{aligned} \frac{1}{r_2^3} = & (\omega_x^2 + \omega_z^2) \left\{ 2 - q^2 \left[\frac{8 \sin^2(\theta)}{(4-a)^2} + \frac{8 \cos^2(\theta)}{(2+a)^2} - \frac{8(17+2a-a^2)}{(4-a)^2(2+a)^2} \right] \right. \\ & \left. + 10q^2 \left[\frac{2 \sin^4(\theta)}{(4-a)^2} + \frac{2 \cos^4(\theta)}{(2+a)^2} - \frac{4(17+2a-a^2) \cos^2(\theta) \sin^2(\theta)}{(4-a)^2(2+a)^2} \right] \right\}^{-1}, \end{aligned} \quad (53)$$

which may now be inserted into (51) to result in a transcendental equation for θ . Figure 5 shows the numerical solutions of the resulting transcendental equation together with the polar angles θ obtained from our numerical simulations of (15). The agreement between our analytical predictions and the numerical simulations is excellent. This shows the remarkable accuracy of the generalized pseudopotential method, which is possible only because the generalized pseudopotential contains hidden physics beyond the standard approach.

V. THREE-ION CRYSTAL MORPHOLOGY

Encouraged by the success of the improved pseudopotential for the two-ion case illustrated in Sec. IV, in this section we now investigate the case of three particles simultaneously stored in the Paul trap, using the improved pseudopotential. The improved, generalized pseudopotential U_{eff} and its 1/length approximated version \tilde{U}_{eff} [see (36) and (37), respectively] for the three particles in the Paul trap are much more complicated than the standard potential

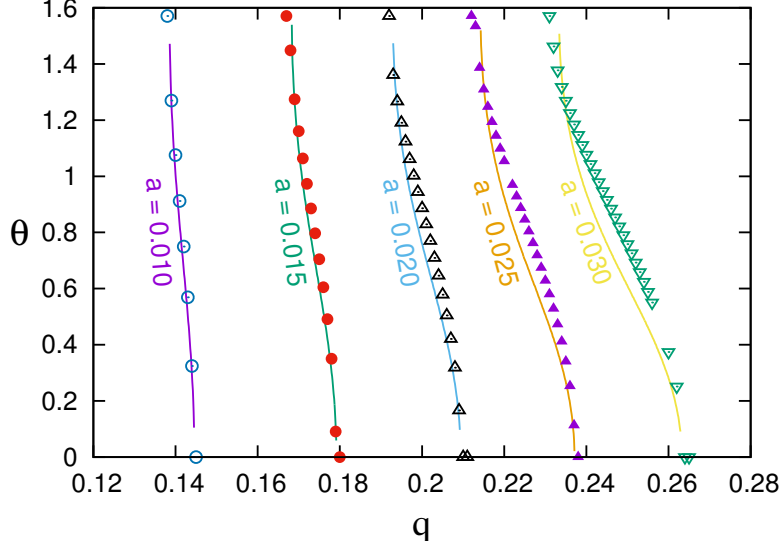


FIG. 5: (Color Online) Polar angle θ of the two-ion tilt phase observed in the Paul trap as a function of q , obtained from numerical simulations of (15). Shown are the cases $a = 0.01$ (open circles), 0.015 (filled circles), 0.02 (open triangles), 0.025 (filled triangles), and 0.03 (open, inverted triangles). Solid lines are the θ solutions of the transcendental equation (51).

$U_{\text{eff}}^{(s)}$ in (34). A natural question to ask is what additional physics and insight we gain from these more complicated expressions. The answer is that, in analogy to the two-ion case, the improved pseudopotential predicts a new regime of crystal morphology that is not captured in the standard approach.

A. Standard vs. generalized pseudopotential prediction

To start, we first investigate the standard potential $U_{\text{eff}}^{(s)}$ in (34). We recall that, to investigate the boundary lines between different crystal morphologies, we need both the first and second derivatives of the potential to be equal to zero. The results for the first derivatives are:

$$\begin{aligned}
 \frac{\partial U_{\text{eff}}^{(s)}}{\partial x} &= \left(-\frac{18}{\rho^3} + \mu_x^2 \right) x = 0, \\
 \frac{\partial U_{\text{eff}}^{(s)}}{\partial y} &= \left(-\frac{2}{\rho^3} - \frac{1}{2r^3} + \mu_y^2 \right) y = 0, \\
 \frac{\partial U_{\text{eff}}^{(s)}}{\partial z} &= \left(-\frac{2}{\rho^3} - \frac{1}{2r^3} + \mu_z^2 \right) z = 0.
 \end{aligned} \tag{54}$$

The results for the second derivatives, including mixed derivatives, are:

$$\begin{aligned}
\frac{\partial^2 U_{\text{eff}}^{(s)}}{\partial x^2} &= 18 \frac{18x^2 - y^2 - z^2}{\rho^5} + \mu_x^2, \\
\frac{\partial^2 U_{\text{eff}}^{(s)}}{\partial y^2} &= 2 \frac{-9x^2 + 2y^2 - z^2}{\rho^5} + \frac{2y^2 - z^2}{2r^5} + \mu_y^2, \\
\frac{\partial^2 U_{\text{eff}}^{(s)}}{\partial z^2} &= 2 \frac{-9x^2 - y^2 + 2z^2}{\rho^5} + \frac{2z^2 - y^2}{2r^5} + \mu_z^2, \\
\frac{\partial^2 U_{\text{eff}}^{(s)}}{\partial x \partial y} &= \frac{54xy}{\rho^5}, \\
\frac{\partial^2 U_{\text{eff}}^{(s)}}{\partial y \partial z} &= \frac{6yz}{\rho^5} + \frac{3yz}{2r^5}, \\
\frac{\partial^2 U_{\text{eff}}^{(s)}}{\partial z \partial x} &= \frac{54zx}{\rho^5}.
\end{aligned} \tag{55}$$

Because of its structure the solutions of the nonlinear system of equations (54) can be classified into the following eight distinct cases:

- case 1: $(x = 0, y = 0, z = 0)$ - Coulomb repulsion, not viable;
- case 2: $(x = 0, y = 0, z \neq 0)$ - Rod phase, observed;
- case 3: $(x = 0, y \neq 0, z = 0)$ - Preferred direction in x - y plane, not viable;
- case 4: $(x = 0, y \neq 0, z \neq 0)$ - Tilted rod phase, not observed;
- case 5: $(x \neq 0, y = 0, z = 0)$ - Preferred direction in x - y plane, not viable;
- case 6: $(x \neq 0, y = 0, z \neq 0)$ - Pop-out phase, observed;
- case 7: $(x \neq 0, y \neq 0, z = 0)$ - Planar phase [symmetry $\rightarrow y = \sqrt{3}x$], observed;
- case 8: $(x \neq 0, y \neq 0, z \neq 0)$ - Tilt phase, observed.

We now investigate cases 2, 6, and 7 in detail, which yields the morphology boundaries between all four observed cases, i.e., cases 2, 6, 7, and 8.

1. Rod phase (case 2)

This case yields $z^3 = 5/[8(q^2 - a)]$. Inserting it into (55) results in zero for all mixed derivatives, and positive for the second derivative in z . Stability is lost in the x and y

directions, respectively, when

$$\begin{aligned}\frac{\partial^2 U_{\text{eff}}^{(s)}}{\partial x^2} = 0 &\rightarrow a = \frac{43}{58}q^2, \\ \frac{\partial^2 U_{\text{eff}}^{(s)}}{\partial y^2} = 0 &\rightarrow a = \frac{1}{2}q^2,\end{aligned}\tag{56}$$

which indicates that the tilted rod phase (case 4), the case where the stability is lost in y , does not occur, because the pop-out phase (case 6), where the stability is lost in x , occurs first, before case 4 can be realized.

2. Pop-out phase (case 6)

This case yields $\rho(y = 0) = \sqrt{9x^2 + z^2} = [3/(a + q^2/2)]^{1/3}$ and $z = [3/(22q^2 - 28a)]^{1/3}$. Inserting these results into (55) results in zero for the x, y and y, z mixed derivatives (and positive for the z, x mixed derivative and second derivatives in x and z). Therefore, stability for this case is lost in y direction, resulting in the tilt-phase (case 8), when

$$\frac{\partial^2 U_{\text{eff}}^{(s)}}{\partial y^2} = 0 \rightarrow a = \frac{1}{2}q^2.\tag{57}$$

3. Planar phase (case 7)

This case yields $y = \sqrt{3}x = [3/(a + q^2/2)]^{1/3}/2$. Inserting this result into (55) results in zero for the y, z and z, x mixed derivatives (and positive for the x, y mixed derivative and second derivatives in x and y). Therefore, stability for this case is lost in z direction, resulting in the tilt phase (case 8), when

$$\frac{\partial^2 U_{\text{eff}}^{(s)}}{\partial z^2} = 0 \rightarrow a = \frac{1}{2}q^2.\tag{58}$$

Comparing the case-6 and the case-8 results, we conclude that the tilt phase, under the conventional, standard pseudopotential, exists only on the line $a = q^2/2$ in the (q, a) control-parameter space. The boundary lines corresponding to the transitions between the four observed crystal morphologies (cases 2, 6, 7, and 8) may be found in Fig. 6.

We now move on to the predictions of the generalized pseudopotential. Starting, this time, with (36), we obtain the boundaries between rod and pop-out, pop-out and tilt, and tilt and planar phases by following exactly the same methodology employed above for the standard pseudopotential, i.e., for the rod and pop-out boundary via eliminating z from

$$\frac{\partial U_{\text{eff}}(x = 0, y = 0, z)}{\partial z} = 0, \quad \left. \frac{\partial^2 U_{\text{eff}}(x, y = 0, z)}{\partial x^2} \right|_{x=0} = 0,\tag{59}$$

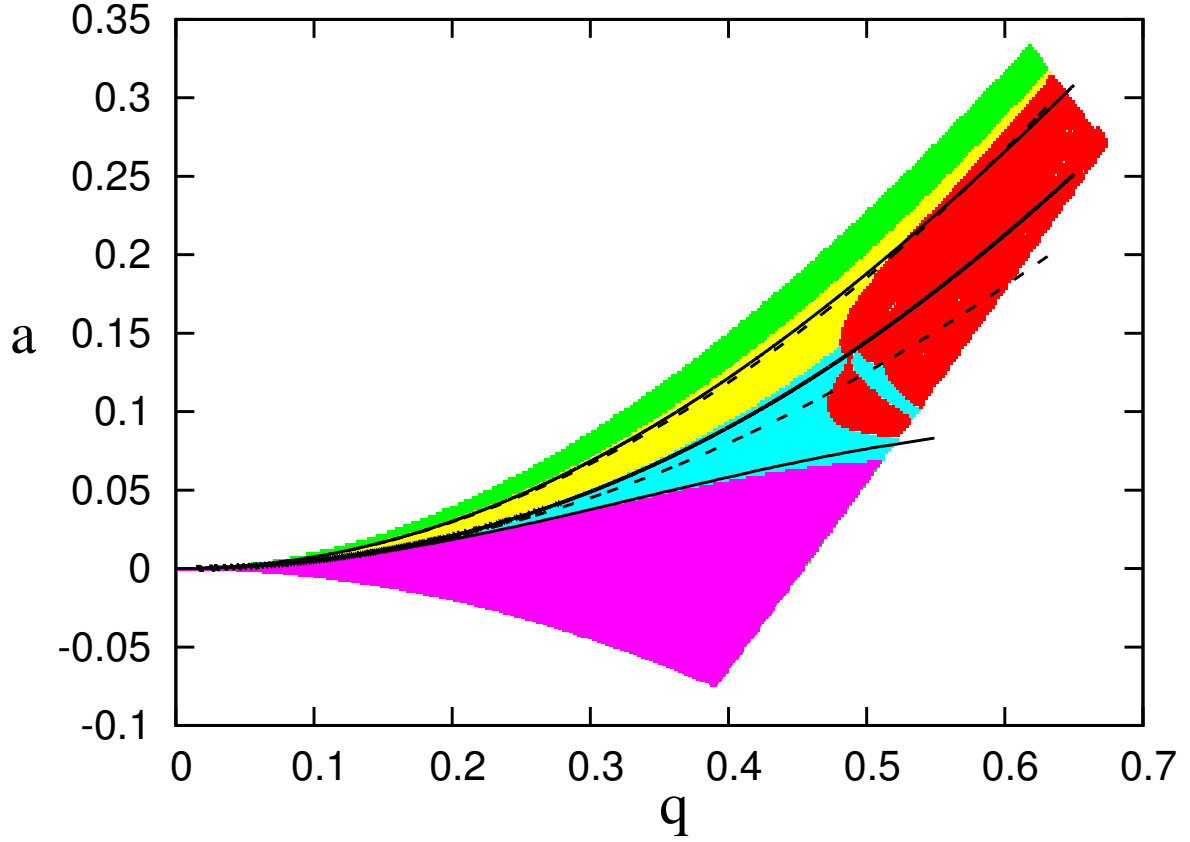


FIG. 6: (Color Online) Standard and improved pseudopotential predictions for three-particle morphology transitions in (q, a) control-parameter space. Green, yellow, blue, and magenta regions denote rod, pop-out, tilt, and planar crystal morphologies, respectively. The red region indicates a region in (q, a) control-parameter space where no stable three-ion crystals exist. The top dashed line is the standard pseudopotential prediction for the rod \leftrightarrow pop-out transition. The standard pseudopotential (incorrectly) predicts that the pop-out \leftrightarrow tilt, and tilt \leftrightarrow planar transitions are degenerate (represented by the bottom dashed line). Solid lines (top to bottom) correspond to the correct predictions of the generalized pseudopotential for rod \leftrightarrow pop-out, pop-out \leftrightarrow tilt, and tilt \leftrightarrow planar transitions.

for the pop-out and tilt boundary via eliminating x and z from

$$\frac{\partial U_{\text{eff}}(x, y=0, z)}{\partial z} = 0, \quad \frac{\partial U_{\text{eff}}(x, y=0, z)}{\partial x} = 0, \quad \frac{\partial^2 U_{\text{eff}}(x, y, z)}{\partial y^2} \Big|_{y=0} = 0, \quad (60)$$

and for the tilt and planar boundary via eliminating x from

$$\frac{\partial U_{\text{eff}}(x, y = \sqrt{3}x, z=0)}{\partial x} = 0, \quad \frac{\partial^2 U_{\text{eff}}(x, y = \sqrt{3}x, z)}{\partial z^2} \Big|_{z=0} = 0. \quad (61)$$

The analytical computation of explicit analytical solutions of the boundaries is not straightforward. Therefore, we compute the solutions of (59), (60), and (61) numerically, which results in the three solid lines in Fig. 6, representing the three boundaries between the four three-particle crystal morphologies. The agreement between the boundary lines between the four different crystal morphologies, determined as a result of our numerical simulations of (15) (green, yellow, blue, and magenta regions in Fig. 6), and the boundary lines predicted by the generalized improved pseudopotential is excellent. The generalized improved pseudopotential, as in the two-particle case discussed in Sec. IV, in contrast to the standard pseudopotential, also predicts both the existence and the location of the new three-particle tilt phase correctly.

B. 1/length approximated generalized pseudopotential

In this subsection, closely following the steps in Sec. V A, we investigate the three-ion crystal in a Paul trap with the help of the 1/length approximated, generalized pseudopotential \tilde{U}_{eff} , defined in (37). In the absence of simple analytical expressions, the motivation behind this approach is to obtain a better analytical handle on the generalized, improved pseudopotential approach.

As will be shown below, while still somewhat complicated, the 1/length approximation yields tractable analytical expressions for the pseudopotential minima and their stability, and thus we are able to determine all boundaries fully analytically.

1. Rod \rightarrow pop-out boundary

Since we start in the rod phase, we have $x = y = 0$ in this case, and we need only

$$\frac{1}{z} \frac{\partial \tilde{U}_{\text{eff}}(x=0, y=0, z)}{\partial z} = \left[-\frac{2}{z^3} - \frac{1}{2z^3} \right] + \frac{4(2q^2 - 2a - a^2)}{2+a} - \frac{q^2}{z^3} \left[\frac{5}{(2+a)^2} \right]. \quad (62)$$

Equating (62) to zero results in

$$z = \left[\frac{10q^2 + 5(2+a)^2}{8(2+a)(2q^2 - 2a - a^2)} \right]^{\frac{1}{3}}. \quad (63)$$

From the standard pseudopotential case we know that the stability of the rod configuration is lost in x -direction. In order to obtain the morphology boundary to the

pop-out phase (case 6), we now evaluate

$$\begin{aligned} \left. \frac{\partial^2 \tilde{U}_{\text{eff}}(x, y=0, z)}{\partial x^2} \right|_{x=0} &= -\frac{18}{z^3} + \frac{6(2q^2 + 4a - a^2)}{4-a} - \frac{45q^2}{z^3} \left[\frac{4}{(2+a)^2} \right] \\ &\quad - \frac{q^2}{z^3} \left[\frac{144(17 + 2a - a^2)}{(4-a)^2(2+a)^2} \right], \end{aligned} \quad (64)$$

which, upon equating it to 0, together with (63), results in

$$\begin{aligned} &q^4(-116a^2 + 3112a - 14048) + q^2(-1328a^3 + 4728a^2 + 13392a - 2752) \\ &+ (29a^6 - 58a^5 - 580a^4 + 232a^3 + 3712a^2 + 3712a) = 0. \end{aligned} \quad (65)$$

This equation can be solved for q^2 using the quadratic solution formula. The result is shown as the top solid line in Fig. 7.

2. Pop-out \rightarrow tilt boundary

Starting in the pop-out phase, we have two degrees of freedom, namely, x and z .

Therefore, we now need

$$\begin{aligned} \frac{1}{x} \frac{\partial \tilde{U}_{\text{eff}}(x, y=0, z)}{\partial x} &= -\frac{6(2q^2 + 4a - a^2)}{4-a} - \frac{18}{(9x^2 + z^2)^{3/2}} \\ &\quad + \frac{144q^2[9(2+a)^2x^2 - (17 + 2a - a^2)z^2]}{(4-a)^2(2+a)^2(9x^2 + z^2)^{5/2}} \\ &\quad - \frac{180q^2[81(2+a)^2x^4 - 18(17 + 2a - a^2)x^2z^2 + (4-a)^2z^4]}{(4-a)^2(2+a)^2(9x^2 + z^2)^{7/2}} \end{aligned} \quad (66)$$

and

$$\begin{aligned} \frac{1}{z} \frac{\partial \tilde{U}_{\text{eff}}(x, y=0, z)}{\partial z} &= -\frac{1}{2z^3} - \frac{q^2}{(2+a)^2z^3} + \frac{4(2q^2 - 2a - a^2)}{2+a} - \frac{2}{(9x^2 + z^2)^{3/2}} \\ &\quad + \frac{16q^2[-9(17 + 2a - a^2)x^2 + (4-a)^2z^2]}{(4-a)^2(2+a)^2(9x^2 + z^2)^{5/2}} \\ &\quad - \frac{20q^2[81(2+a)^2x^4 - 18(17 + 2a - a^2)x^2z^2 + (4-a)^2z^4]}{(4-a)^2(2+a)^2(9x^2 + z^2)^{7/2}} \end{aligned} \quad (67)$$

for the first derivatives, and

$$\begin{aligned} \left. \frac{\partial^2 \tilde{U}_{\text{eff}}(x, y, z)}{\partial y^2} \right|_{y=0} &= \frac{2(2q^2 + 4a - a^2)}{4-a} - \frac{1}{2z^3} - \frac{5q^2}{(2+a)^2z^3} - \frac{4(17 + 2a - a^2)q^2}{(4-a)^2(2+a)^2z^3} \\ &\quad - \frac{2}{(9x^2 + z^2)^{3/2}} + \frac{16q^2[9(2+a)^2x^2 - (17 + 2a - a^2)z^2]}{(4-a)^2(2+a)^2(9x^2 + z^2)^{5/2}} \\ &\quad - \frac{20q^2[81(2+a)^2x^4 - 18(17 + 2a - a^2)x^2z^2 + (4-a)^2z^4]}{(4-a)^2(2+a)^2(9x^2 + z^2)^{7/2}} \end{aligned} \quad (68)$$

for the second derivative. The transition from the pop-out phase to the tilt-phase is observed when the pop-out crystal loses its stability in y -direction.

Now, subtracting 9 times (68) from (66) results in

$$z = \left\{ \frac{3}{8(2q^2 + 4a - a^2)} \left[(4 - a) + \frac{2q^2}{4 - a} + \frac{72q^2}{(2 + a)^2} \right] \right\}^{1/3}. \quad (69)$$

Subtracting (66) from 9 times (67) and rearranging terms results in

$$\delta(9x^2 + z^2)^{5/2} = \beta x^2 + \gamma, \quad (70)$$

where

$$\begin{aligned} \delta &= \frac{9}{2z^3} + \frac{9q^2}{(2 + a)^2 z^3} + 42a + 12q^2 \left[\frac{1}{4 - a} - \frac{6}{2 + a} \right], \\ \beta &= -\frac{3888(7 + 2a)q^2}{(4 - a)^2(2 + a)^2}, \\ \gamma &= \frac{432(11 - 2a)q^2 z^2}{(4 - a)^2(2 + a)^2}. \end{aligned} \quad (71)$$

At this point, together with z in (69), we realize that (70) is a quintic equation in x^2 . A detailed discussion of how to obtain the desired root may be found in Appendix C. We find

$$x = z \sqrt{\frac{11 - 2a}{9(7 + 2a)}}, \quad (72)$$

which, together with (69), may now be used to result in a single analytical expression that relates q and a , which yields the pop-out \rightarrow tilt boundary line:

$$\begin{aligned} &3(4 - a)^3 a(2 + a)^3 - 8(4 - a)(2 + a)(12 - 92a + 17a^2)q^2 \\ &- 4(1064 - 580a + 86a^2 - 3a^3)q^4 = 0. \end{aligned} \quad (73)$$

Using the quadratic solution formula, we may now solve for q^2 . The resulting boundary is shown in Fig. 7 as the second solid line from the top.

3. Planar \rightarrow tilt boundary

In order to access the third and last boundary, we evaluate

$$\frac{1}{x} \frac{\partial \tilde{U}_{\text{eff}}(x = 0, y = \sqrt{3}x, z = 0)}{\partial x} = -\frac{\sqrt{3}}{2x^3} - \frac{\sqrt{3}q^2}{(4 - a)^2 x^3} + \frac{12(2q^2 + 4a - a^2)}{4 - a} \quad (74)$$

and

$$\left. \frac{\partial^2 \tilde{U}_{\text{eff}}(x, y = \sqrt{3}x, z)}{\partial z^2} \right|_{z=0} = -\frac{\sqrt{3}}{12x^3} + \frac{4(2q^2 - 2a - a^2)}{2+a} - \frac{\sqrt{3}q^2}{2(4-a)^2x^3} + \frac{\sqrt{3}q^2}{3(2+a)^2x^3} - \frac{18\sqrt{3}q^2}{(4-a)^2(2+a)^2x^3}. \quad (75)$$

Setting both (74) and (75) equal to zero, then eliminating x , we obtain the 1/length approximated improved pseudopotential prediction of the tilt-planar boundary of three particles stored in the Paul trap according to

$$a(2+a)^2(4-a)^3 + 8(4-a)(4-9a-4a^2)q^2 - 4(24+8a+a^2)q^4 = 0, \quad (76)$$

which, as in case 2 above, may be solved for q^2 with the help of the quadratic solution formula. The result is shown as the bottom solid line in Fig. 7.

C. Doubly-approximated pseudopotential prediction

Explicit expressions of the boundaries $a_{\text{boundary}}(q)$ between rod and pop-out, and tilt and planar phases may be obtained by further approximating \tilde{U}_{eff} in (37) up to first order in a and employing the same methodology used in Secs. V A and V B. Denoting the doubly-approximated improved potential as $\tilde{U}_{\text{eff}}^{(\text{app})}$, we obtain

$$\begin{aligned} \tilde{U}_{\text{eff}}^{(\text{app})} = & \left[\frac{2}{\rho} + \frac{1}{2r} \right] + \left[\frac{3q^2}{2} + 3a + \frac{3aq^2}{8} \right] x^2 + \left[\frac{q^2}{2} + a + \frac{aq^2}{8} \right] y^2 + [2q^2 - 2a - aq^2] z^2 \\ & + \frac{q^2}{\rho^5} \left[\frac{81x^4}{4} \left(1 + \frac{a}{2} \right) + \frac{y^4}{4} \left(1 + \frac{a}{2} \right) + z^4(1-a) + \frac{9x^2y^2}{2} \left(1 + \frac{a}{2} \right) - \frac{y^2z^2}{8} \left(17 - \frac{13a}{2} \right) \right. \\ & \left. - \frac{9z^2x^2}{8} \left(17 - \frac{13a}{2} \right) \right] + \frac{q^2}{r^5} \left[\frac{y^4}{16} \left(1 + \frac{a}{2} \right) + \frac{z^4}{4}(1-a) - \frac{y^2z^2}{32} \left(17 - \frac{13a}{2} \right) \right]. \end{aligned} \quad (77)$$

(i) Rod \rightarrow pop-out boundary

Repeating the above procedure, we obtain

$$\frac{1}{z} \left. \frac{\partial \tilde{U}_{\text{eff}}^{(\text{app})}(x=0, y=0, z)}{\partial z} \right|_{z=0} = -\frac{5}{2z^3} + 2(2q^2 - 2a - aq^2) - \frac{5(1-a)q^2}{4z^3} \quad (78)$$

and

$$\left. \frac{\partial^2 \tilde{U}_{\text{eff}}(x, y=0, z)}{\partial x^2} \right|_{x=0} = 2 \left(3a + \frac{3q^2}{2} + \frac{3aq^2}{8} \right) - \frac{18}{z^3} - \frac{9 \left(17 - \frac{13a}{2} \right) q^2}{4z^3} - \frac{45(1-a)q^2}{z^3}. \quad (79)$$

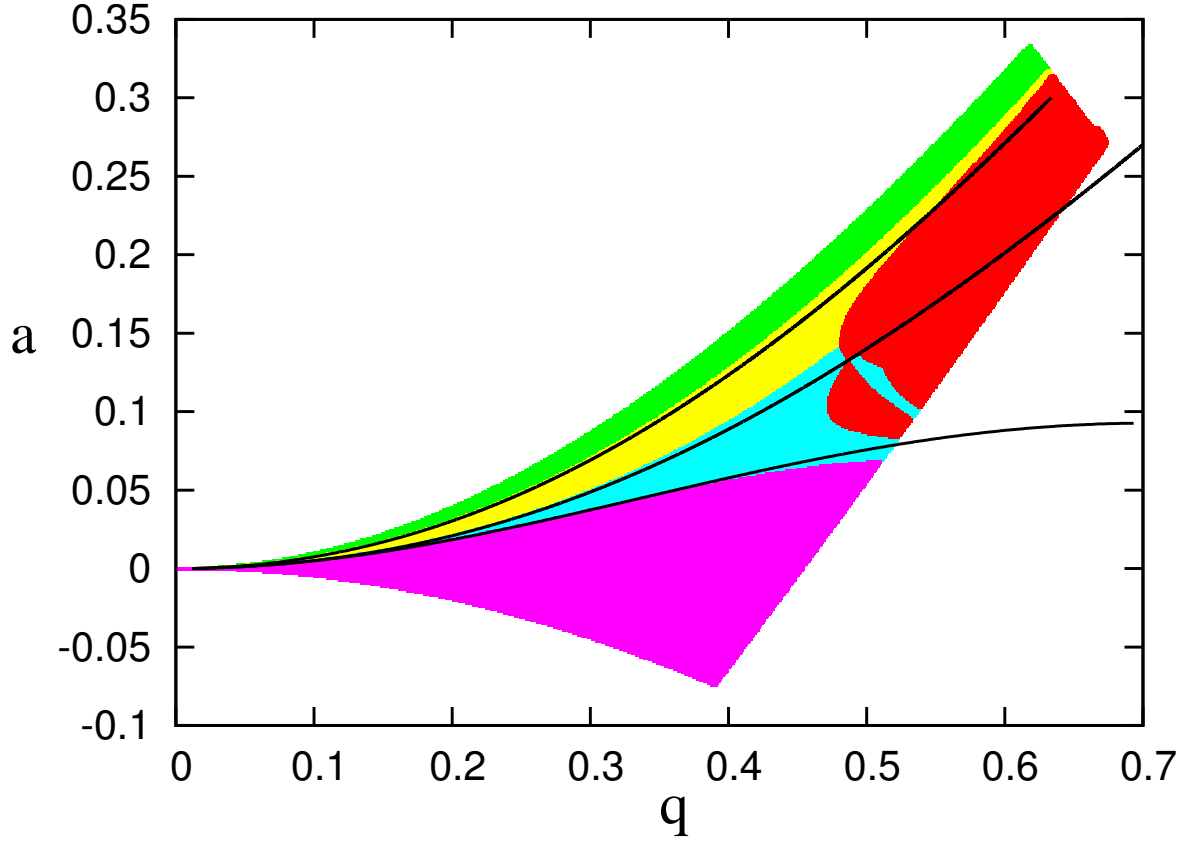


FIG. 7: (Color Online) Improved, 1/length approximated generalized three-ion pseudopotential prediction of crystal morphology transitions in (q, a) control-parameter space. Colored areas code for the four observed three-particle crystal morphologies. They are imported from Fig. 6 without any modifications. Solid lines are the analytical predictions of the boundary lines between the four three-particle crystal morphologies as computed in Sec. VB.

Equating the two equations (78) and (79) to zeros and eliminating z results in

$$4q^2(86 + 439q^2) + a^2q^2(1312 + 641q^2) - a(464 + 2018q^2 + 2145q^4) = 0, \quad (80)$$

which yields the small- a , 1/length approximated improved pseudopotential three-particle rod \rightarrow pop-out boundary line

$$a_{\text{rod} \rightarrow \text{pop-out}}(q) = [464 + 2018q^2 + 2145q^4 - (215296 + 1872704q^2 + 4257572q^4 - 1440284q^6 + 98641q^8)^{1/2}] / (2624q^2 + 1282q^4). \quad (81)$$

(ii) Pop-out \rightarrow tilt boundary

This time, we start with

$$\begin{aligned}
\frac{1}{x} \frac{\partial \tilde{U}_{\text{eff}}^{(\text{app})}(x, y=0, z)}{\partial x} &= -\frac{18}{(9x^2 + z^2)^{3/2}} + \left[3q^2 + 6a + \frac{3aq^2}{4} \right] \\
&\quad - \frac{45q^2}{(9x^2 + z^2)^{7/2}} \left[\frac{81x^4}{4} \left(1 + \frac{a}{2} \right) + z^4(1-a) - \frac{9x^2z^2}{8} \left(17 - \frac{13a}{2} \right) \right] \\
&\quad + \frac{q^2}{(9x^2 + z^2)^{5/2}} \left[81x^2 \left(1 + \frac{a}{2} \right) - \frac{9z^2}{4} \left(17 - \frac{13a}{2} \right) \right] \\
&= 0, \\
\frac{1}{z} \frac{\partial \tilde{U}_{\text{eff}}^{(\text{app})}(x, y=0, z)}{\partial z} &= -\frac{1}{2z^3} - \frac{2}{(9x^2 + z^2)^{3/2}} + [4q^2 - 4a - 2aq^2] \\
&\quad - \frac{5q^2}{(9x^2 + z^2)^{7/2}} \left[\frac{81x^4}{4} \left(1 + \frac{a}{2} \right) + z^4(1-a) - \frac{9x^2z^2}{8} \left(17 - \frac{13a}{2} \right) \right] \\
&\quad + \frac{q^2}{(9x^2 + z^2)^{5/2}} \left[4z^2(1-a) - \frac{9x^2}{4} \left(17 - \frac{13a}{2} \right) \right] - \frac{q^2}{z^3} \frac{1-a}{4} \\
&= 0, \tag{82}
\end{aligned}$$

for the first derivatives, and

$$\begin{aligned}
\left. \frac{\partial^2 \tilde{U}_{\text{eff}}^{(\text{app})}(x, y, z)}{\partial y^2} \right|_{y=0} &= -\frac{1}{2z^3} - \frac{q^2}{16z^3} \left[\left(17 - \frac{13a}{2} \right) + 20(1-a) \right] - \frac{2}{(9x^2 + z^2)^{3/2}} \\
&\quad + \frac{q^2}{(9x^2 + z^2)^{5/2}} \left[9 \left(1 + \frac{a}{2} \right) x^2 - \frac{1}{4} \left(17 - \frac{13a}{2} \right) z^2 \right] \\
&\quad - \frac{5q^2}{(9x^2 + z^2)^{7/2}} \left[\frac{81}{4} \left(1 + \frac{a}{2} \right) x^4 - \frac{9}{8} \left(17 - \frac{13a}{2} \right) x^2 z^2 + (1-a)z^4 \right] \\
&= 0 \tag{83}
\end{aligned}$$

for the second derivative. Subtracting 9 times (83) from (82) results in

$$z = \left[\frac{3(16 + 74q^2 - 53aq^2)}{16(8a + 4q^2 + aq^2)} \right]^{1/3}. \tag{84}$$

Subtracting 9 times the second equation of (82) from the first equation of (82) and rearranging terms results in an equation of the form (70), where

$$\begin{aligned}
\delta &= \mu_x^2 - 9\mu_z^2 + \frac{75}{4}aq^2 + \frac{9}{2z^3}, \\
\beta &= -q^2 \left[81 \left(1 + \frac{a}{2} \right) + \frac{81}{4} \left(17 - \frac{13a}{2} \right) \right], \\
\gamma &= q^2 \left[\frac{9z^2}{4} \left(17 - \frac{13a}{2} \right) + 36z^2(1-a) \right]. \tag{85}
\end{aligned}$$

As in the analogous case discussed in Sec. VB, following the detailed discussion in Appendix C, we find

$$x = z \sqrt{\frac{5}{9} - \frac{16}{42 - 9a}}, \quad (86)$$

which, together with z in (84), results in the pop-out \rightarrow tilt boundary line

$$a_{\text{pop-out} \rightarrow \text{tilt}} = \frac{576 + 2288q^2 + 2091q^4 - \sqrt{331776 + 2635776q^2 + 5934208q^4 - 858592q^6 + 58081q^8}}{53(56q^2 + 25q^4)}. \quad (87)$$

(iii) Planar \rightarrow tilt boundary

For the third and last boundary, i.e., the one between the tilt and planar phases, we begin with

$$\begin{aligned} \left. \frac{1}{x} \frac{\partial \tilde{U}_{\text{eff}}^{(\text{app})}}{\partial x} \right|_{z=0, y=\sqrt{3}x} &= -\frac{\sqrt{3}}{2x^3} - \frac{\sqrt{3}q^2}{16x^3} \left(1 + \frac{a}{2}\right) \\ &+ 6 \left(a + \frac{q^2}{2} + \frac{aq^2}{8}\right) + 2 \left(3a + \frac{3q^2}{2} + \frac{3aq^2}{8}\right) = 0 \end{aligned} \quad (88)$$

and

$$\begin{aligned} \left. \frac{\partial^2 \tilde{U}_{\text{eff}}^{(\text{app})}}{\partial z^2} \right|_{z=0, y=\sqrt{3}x} &= 2(-2a + 2q^2 - aq^2) - \frac{1}{4\sqrt{3}x^3} \\ &- \frac{q^2}{32\sqrt{3}x^3} \left(17 - \frac{13a}{2}\right) - \frac{5q^2}{32\sqrt{3}x^3} \left(1 + \frac{a}{2}\right) = 0. \end{aligned} \quad (89)$$

Eliminating x from (88) and (89), we obtain

$$4q^2a^2 + 4(4 - 3q^2)q^2 - a[32 + q^2(44 + q^2)] = 0, \quad (90)$$

which may be solved explicitly for a to result in

$$a_{\text{tilt} \rightarrow \text{planar}} = \frac{32 + 44q^2 + q^4 - \sqrt{1024 + 2816q^2 + 1744q^4 + 280q^6 + q^8}}{8q^2}. \quad (91)$$

All boundaries (i)-(iii), together with our simulation results, are presented in Fig. 8. The agreement between the predicted boundaries and numerical results is excellent, in particular for small a . For $q < 0.4$, e.g., the analytical boundaries fall within 5% of the exact, numerically computed boundaries.

VI. FOUR-ION CRYSTAL MORPHOLOGIES

With increasing N , as is already apparent in Sec. V for the case of three particles, analytical analysis of the crystal configurations becomes an increasingly difficult task to

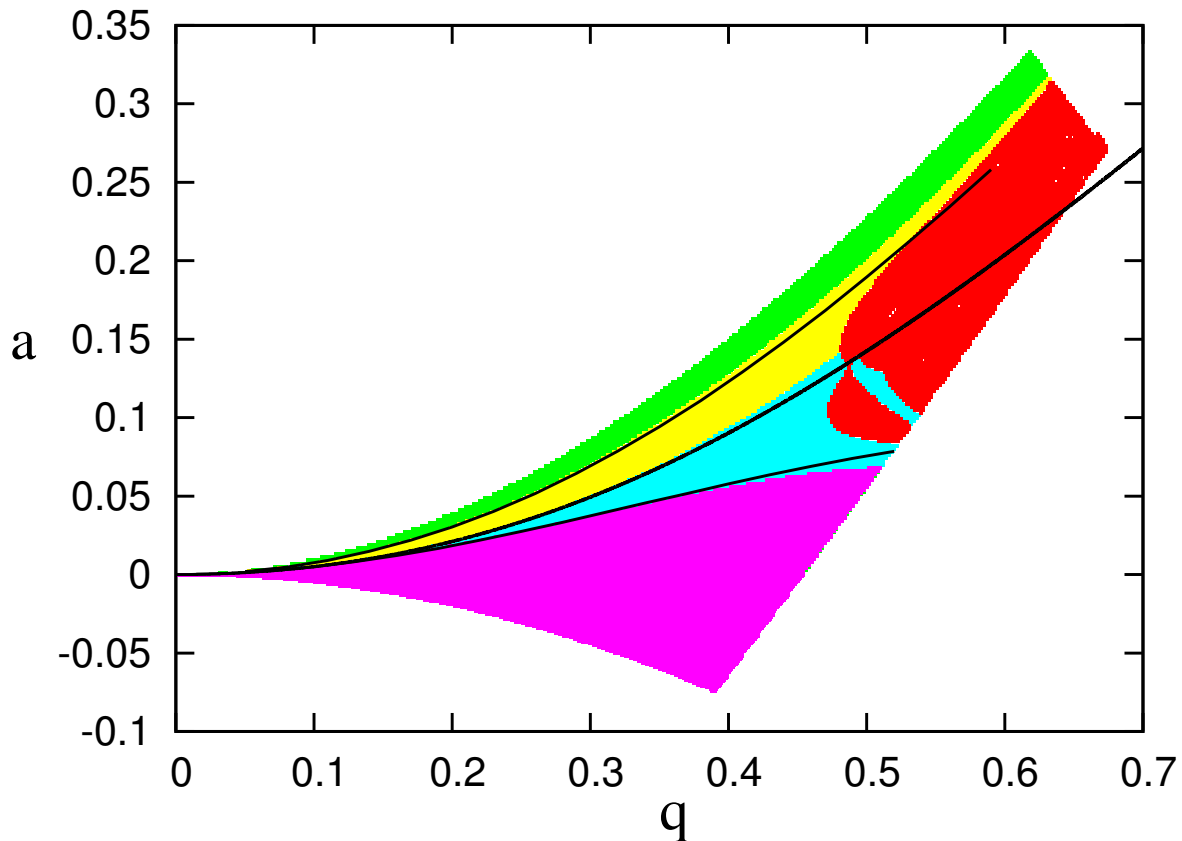


FIG. 8: (Color Online) Improved, $1/\text{length}$, small- a approximated generalized three-ion pseudopotential prediction of morphology boundaries (solid lines) predicted in Sec. VC in the (q, a) control-parameter space. Color codes for the three-particle morphologies are the same as those used in Figs. 6 and 7.

perform. Thus, in this section, where we focus on the case $N = 4$, we primarily present numerical results.

Figure 9 shows the observed crystal orientations obtained from our numerical simulations. As detailed in Figs. 9(a)-(g), we observe seven different morphologies. Among them, the most general configuration is shown in panel (e), which we magnified in relation to the other six morphologies illustrated in Fig. 9 to show our choice of position coordinates, x, y, z, v , and w , for the $N = 4$ case.

Numerical results for locations and types of four-ion crystal morphologies are shown in Fig. 10 along with the numerical solutions of the boundaries between them, following the general analytical framework available in Appendix A, applied to the four-particle case. The

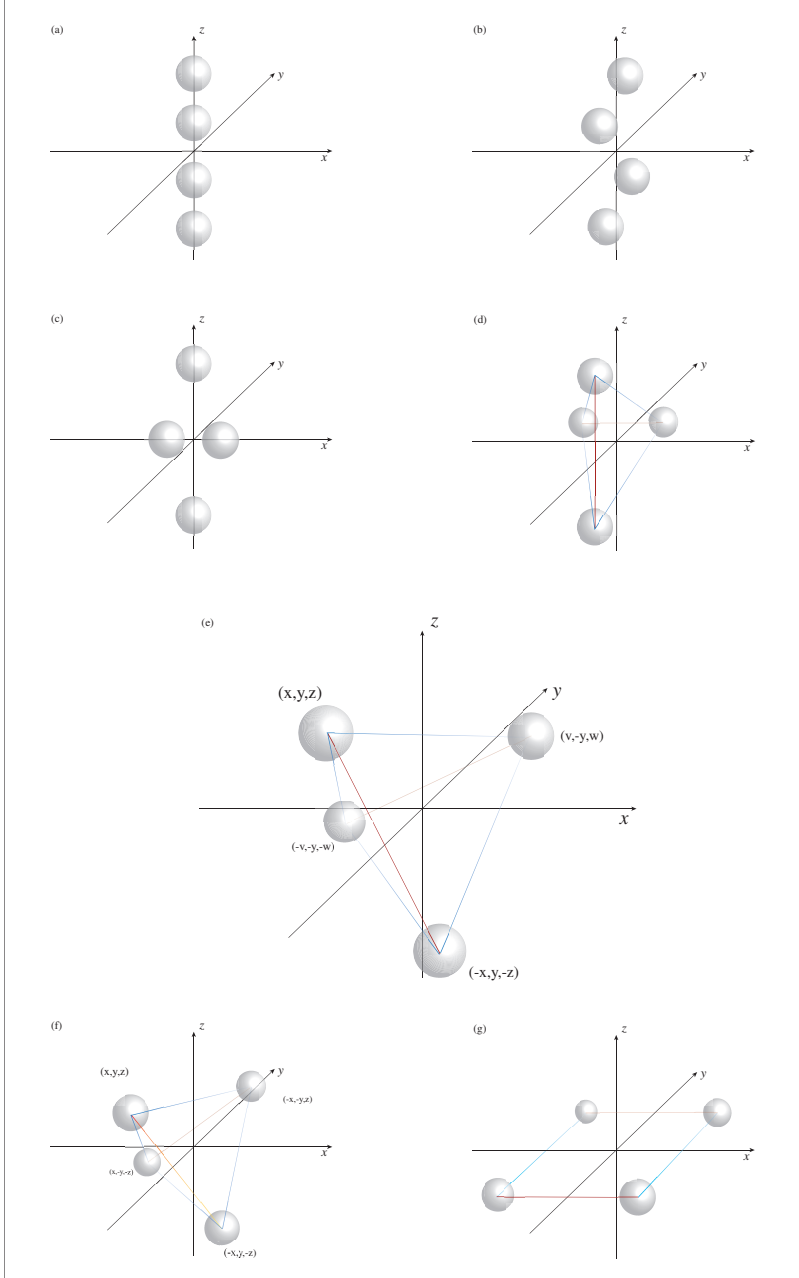


FIG. 9: The seven possible crystal configurations of four charged particles stored in a Paul trap. Panel (e) represents the most general configuration, wherein our position-parameter choice appears. Lines drawn between particles in panels (d)-(g) are to guide the eye.

stability assessment of each crystal configuration is based on the Hessian matrix [30, 35], defined as $H_{ij} = \partial^2 U_{\text{eff}} / \partial i \partial j$, where $i, j \in \{x, y, z, v, w\}$. Except for one, which corresponds to the metamorphosis between the configurations shown in panels (d) and (e) of Fig. 9, all morphology boundaries were determined via the Hessian method. The numerically evaluated

analytical boundaries match the results of our numerical simulations of (15) to an excellent degree of accuracy.

In contrast, in Fig. 11, we show the boundary lines expected from the standard pseudopotential framework. As in the case of the generalized pseudopotential, we used the Hessian to numerically evaluate the resulting analytical boundaries. Once again, our method results in all morphology boundaries except for the one that corresponds to the metamorphosis between the configurations shown in panels (d) and (e) of Fig. 9. Expectedly so, and in contrast to our improved pseudopotential, the standard pseudopotential fails to predict many of the boundaries observed in our numerical simulations. Once again, this corroborates the power of the generalized pseudopotential, accurately predicting the morphology boundaries of four-ion crystals in the Paul trap.

VII. DISCUSSION

At the beginning of the 20th century, prompted by the eminent mathematician David Hilbert (of Hilbert-space fame), Föppl [36] was the first to investigate analytically crystalline structures of charged particles in a harmonic-oscillator potential. At that time, the physical application of charged-particle crystals was not to traps but to atomic structure, since, according to Thomson’s plum-pudding model, the prevailing atomic model at the beginning of the 20th century, electrons were thought to be embedded in a positively charged sphere, and the groundstate of atoms was thought to be formed by the crystalline structures of electrons in this positive background charge. Since, according to Maxwell’s theory, already highly developed at the time, a homogeneously charged sphere corresponds to a harmonic oscillator potential, by computing crystalline electron structures in an isotropic oscillator potential, Föppl had, in fact, solved the atomic structure problem of his time. While, these days, our atomic models differ quite a bit from the atomic models prevailing at Föppl’s time, in connection with quantum dots [37], sometimes called “artificial atoms” [38], Thomson’s plum-pudding model has recently experienced a renaissance. Quantum dots have numerous applications in physics and technology since, among others applications, they may act as transistors, solar cells, and lasers [37]. In essence, a quantum dot is a nano-scale semiconductor trap, capable of confining electrons in all three spatial dimensions. To lowest order, the electric potential confining the electrons in the quantum dot is a harmonic oscillator po-

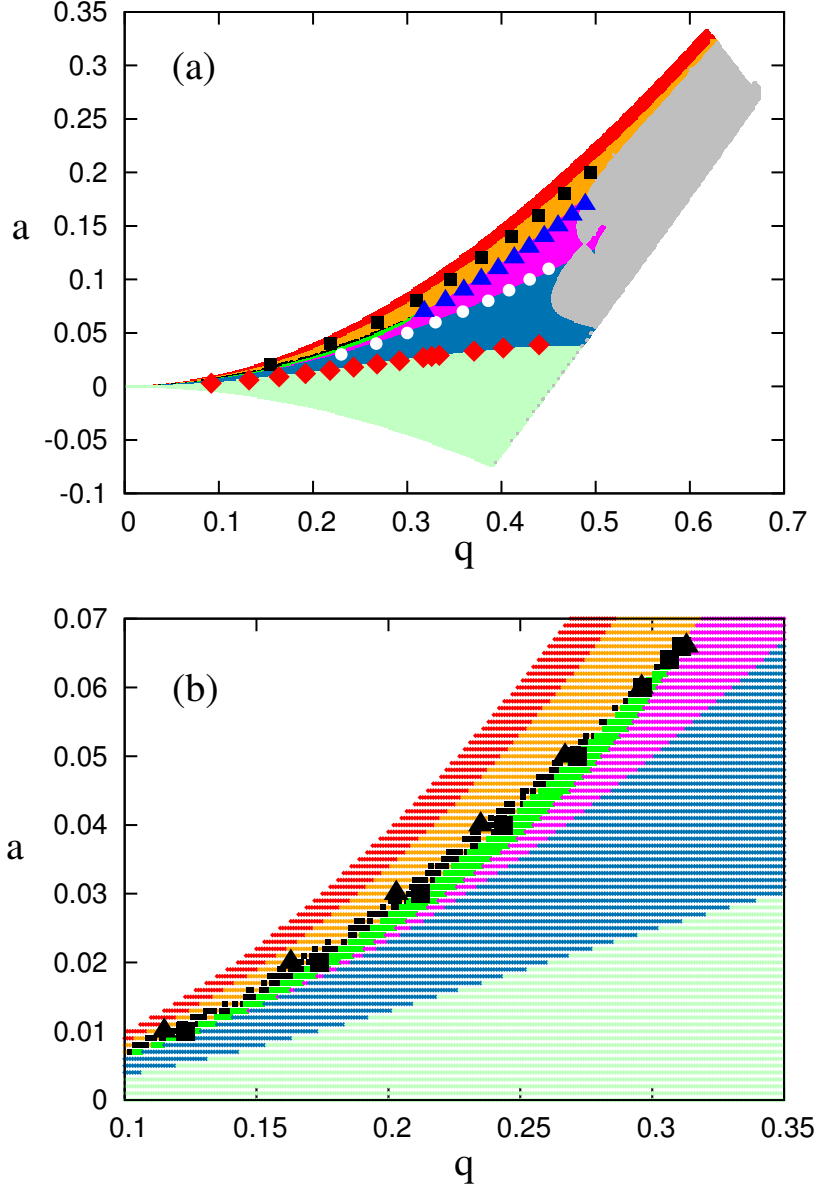


FIG. 10: (Color online) Crystal morphologies according to our numerical simulations of (15) (colored regions) and their boundaries, predicted by the generalized pseudopotential (plot symbols), for $N = 4$. The results for the full stability region are shown in (a); (b) shows a zoom of the region $0.1 \leq q \leq 0.35$, $0 \leq a \leq 0.07$. The morphologies shown in panels (a)-(g) of Fig. 9 correspond to the colors in the order of red, orange, black, green, magenta, blue, and light green. The analytical, generalized pseudopotential predictions of the boundaries between the different morphologies are indicated by the plot symbols in panels (a) and (b): squares, triangles, circles, and diamonds in (a) indicate the red \leftrightarrow orange, orange \leftrightarrow magenta, magenta \leftrightarrow blue, and blue \leftrightarrow light-green boundaries, respectively. Triangles and squares in (b) indicate orange \leftrightarrow black and black \leftrightarrow green boundaries, respectively.

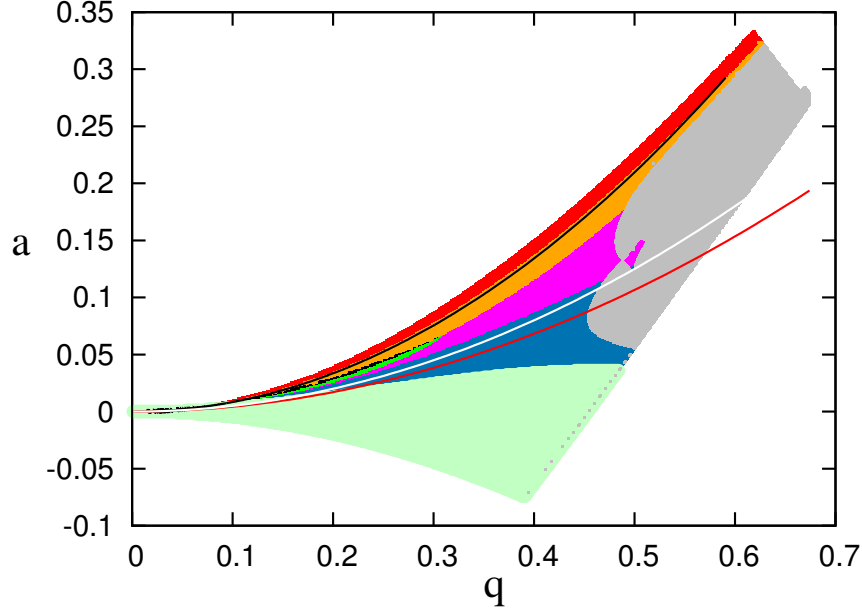


FIG. 11: (Color online) $N = 4$ crystal morphologies (colored regions) and their boundaries (solid lines) predicted by the standard pseudopotential. The color codes for the morphologies are identical to those in Fig. 10. The black line denotes the prediction of the standard pseudopotential for the boundary between red and orange; the white line, $a = q^2/2$, denotes the (degenerate) prediction of the standard pseudopotential for the boundaries between orange and black, orange and magenta, and magenta and blue; the red line denotes the predicted boundary between blue and light green. The predicted boundary between black and green lies outside the (q, a) control-parameter region shown in the figure.

tential. Thus, a quantum dot may be considered a realization of Thomson’s plum-pudding model, which, unexpectedly, returns Föppl’s work [36], published more than a century ago, to the front burner.

Föppl’s electron crystals are relevant in our context, since they describe the crystalline structures expected in what we call the standard pseudopotential. Our work, however, reported in this paper, goes beyond Föppl’s work in that we consider crystalline structures in the cylindrically symmetric, but highly deformed, improved pseudopotentials. For these potentials, we succeeded to compute and classify the structures of all two-, three-, and four-ion crystals and their boundaries as a function of the Paul-trap control parameters a and q .

Unlike Föppl’s work [36], or the work on quantum dots [37, 38], our starting point is not a time-independent potential. Quite the contrary. Our starting point are the periodically driven, time-dependent equations of motion (15), for which a time-independent potential first has to be derived. In the Introduction of this paper (Sec. I) we saw that, for periodically driven quantum systems, in the stroboscopic picture, a time-independent Hamiltonian always exists (the quasi-energy operator), but that for nonlinear, classical systems, the existence of a meaningful time-independent Hamiltonian, in analogy to the quantum quasi-energy operator, cannot be guaranteed. Thus, by constructing the higher-order improved pseudopotentials and by showing that the crystals structures obtained in the pseudopotential picture reproduce all crystal structures seen in the (numerically) exact simulations of (15), we showed that pseudopotentials for periodically driven, nonlinear systems can indeed be constructed in a systematic way.

Loosely speaking, we carried our systematic expansions “up to second order” by including not only $\cos(2\tau)$ terms in our analytical derivations, which yields the standard pseudopotential, but also $\cos(4\tau)$ terms, which, upon averaging, yield our improved pseudopotentials. It is this improvement step that is capable of capturing all crystal configurations, in contrast with the standard, lower-order standard pseudopotential, which did not catch many of the more “exotic” crystal morphologies. In addition, the boundary lines between different crystal morphologies are near perfectly predicted by our improved pseudopotential.

However, there is one essential limitation of our improved pseudopotential. Even our improved pseudopotential does not predict the existence of the red regions in Figs. 4, 6, 7, and 8, where no crystals exist. This may be beyond the power of even higher-order pseudopotentials, since the red regions in Figs. 4, 6, 7, and 8 represent regions of dynamical chaos [39] which are hard to represent with smooth potentials. This is not to say that time-independent potentials cannot produce chaos. Quite the contrary. Many examples are known, for instance the potential of the diamagnetic hydrogen atom [40] in AMO physics, which produces chaotic motions of the hydrogenic electron in a combination of the Coulomb field and an externally applied, static magnetic field. However, our potentials are different. They are supposed to accurately represent the macromotion positions at the stroboscopic times of the system, a task that is impossible to perform in the case of chaotic motion unless the potential itself has a “chaotic” structure. Nevertheless, one important property of the red regions in Figs. 4, 6, 7, and 8 is that as a prerequisite for the absence of crystals in

these regions, period-one fixed points [39] need to lose their stability. This should be within the power of the pseudopotential approach, but needs to await expansions to even higher orders, since explicit investigations of fixed-point stability in the red regions show that even our improved pseudopotential still predicts (erroneously) stability of period-one fixed points in this region. A period-one fixed-point analysis on the basis of the full time-dependent equations of motion (15) showed explicitly that these fixed points are indeed unstable in the red regions in Figs. 4, 6, 7, and 8.

VIII. SUMMARY AND CONCLUSION

One can be seriously misled by the predictions of the standard Paul-trap pseudopotential, which, e.g., fails to predict the existence of any of the more “exotic” ion crystal configurations in the Paul trap. This is the primary reason for why, in this paper, we developed an improved pseudopotential, whose predictive power was tested for two, three, and four simultaneously stored ions in the Paul trap. Unlike the standard pseudopotential, used by many researchers, the improved pseudopotential is capable of predicting, without fail, any of the many three- and four-ion crystal morphologies in the Paul trap, including the boundaries between these crystal structures in the (q, a) control-parameter space of the Paul trap. Most of the three- and four-particle crystal structures predicted in our paper have never been seen experimentally. Many laboratories throughout the world have the ability to investigate and image few-ion systems in the Paul trap. We are looking forward to the experimental verification of the ion-crystal morphologies and the transitions between them predicted in this paper.

Appendix A: n -coordinate framework

In this appendix, we derive a general, n -coordinate analytical framework that may be used to result in the improved pseudopotential expressions for any number of particles in the Paul trap. We start with the n coupled differential equations

$$m_{X^{(i)}} \ddot{X}^{(i)} = -U_{X^{(i)}}(X^{(1)}, X^{(2)}, \dots, X^{(n)}) - k_{X^{(i)}} X^{(i)} \cos(\omega t), \quad (\text{A1})$$

where $m_{X^{(i)}}$ are the effective masses corresponding to the coordinates $X^{(i)}$, $U_{X^{(i)}} = \partial U / \partial X^{(i)}$, and $k_{X^{(i)}}$ are constants. Denoting

$$X^{(i)}(t) = x^{(i)}(t) + \xi^{(i)} \cos(\omega t), \quad (\text{A2})$$

assuming $\xi^{(i)}$ is small compared to $x^{(i)}(t)$, and $x^{(i)}(t)$ varies slowly compared to the timescale of $\cos(\omega t)$, we may expand $U_{X^{(i)}}(X^{(1)}, X^{(2)}, \dots, X^{(n)})$ in $\xi^{(i)}(t)$ according to

$$\begin{aligned} U(X^{(1)}, X^{(2)}, \dots, X^{(n)}) &\approx U(x^{(1)}, x^{(2)}, \dots, x^{(n)}) \\ &+ \sum_{i=1}^n U_{x^{(i)}} \xi^{(i)} \cos(\omega t) + \sum_{i,j} \frac{1}{2} U_{x^{(i)}x^{(j)}} \xi^{(i)} \xi^{(j)} \cos^2(\omega t), \end{aligned} \quad (\text{A3})$$

where $U_{x^{(i)}x^{(j)}} = \partial^2 U / \partial x^{(i)} \partial x^{(j)}$, evaluated at $X^{(i)} = x^{(i)}$ and $X^{(j)} = x^{(j)}$. With (A3), we may write

$$\begin{aligned} U_{X^{(i)}} &= U_{x^{(i)}} + \sum_{j=1}^n U_{x^{(j)}x^{(i)}} \xi^{(j)} \cos(\omega t) \\ &+ \frac{1}{2} \sum_{j,k} U_{x^{(k)}x^{(j)}x^{(i)}} \xi^{(k)} \xi^{(j)} \cos^2(\omega t), \end{aligned} \quad (\text{A4})$$

which may then be inserted into (A1) to result in

$$m_{X^{(i)}} \omega^2 \xi^{(i)} = \sum_{j=1}^n U_{x^{(j)}x^{(i)}} \xi^{(j)} + k_{X^{(i)}} x^{(i)} \quad (\text{A5})$$

upon comparing coefficients of corresponding powers of $\cos(\omega t)$. Since (A5) is a system of n coupled linear equations in $\xi^{(i)}$, denoting \mathcal{A} as the matrix whose matrix elements are

$$\mathcal{A}_{ij} = \begin{cases} m_{X^{(i)}} \omega^2 - U_{x^{(i)}x^{(i)}} & \text{if } i = j, \\ -U_{x^{(j)}x^{(i)}} & \text{if } i \neq j, \end{cases} \quad (\text{A6})$$

and denoting $\vec{\xi} = (\xi^{(1)}, \xi^{(2)}, \dots, \xi^{(n)})^T$ and $\vec{b} = (k_{X^{(1)}} x^{(1)}, k_{X^{(2)}} x^{(2)}, \dots, k_{X^{(n)}} x^{(n)})^T$, we obtain the i th element $\xi^{(i)}$ of $\vec{\xi}$ using Cramer's rule [41]

$$\xi^{(i)} = \frac{\det(\mathcal{A}_i)}{\det(\mathcal{A})}, \quad (\text{A7})$$

where $\det(\dots)$ denotes the determinant of the matrix argument and \mathcal{A}_i is the matrix whose i th column is \vec{b} but otherwise the same as matrix \mathcal{A} . Averaging (A1) over one cycle of $\cos(\omega t)$, with (A7), the effective equations of motion become

$$m_{X^{(i)}} \ddot{x}^{(i)} = -U_{x^{(i)}} - \frac{1}{4} \sum_{j,k} U_{x^{(k)}x^{(j)}x^{(i)}} \xi^{(k)} \xi^{(j)} - \frac{1}{2} k_{X^{(i)}} \xi^{(i)}, \quad (\text{A8})$$

which can be shown by direct differentiation to have the effective potential

$$U_{\text{eff}}(x^{(1)}, x^{(2)}, \dots, x^{(n)}) = U(x^{(1)}, x^{(2)}, \dots, x^{(n)}) + \frac{1}{4} \sum_i k_{X^{(i)}} x^{(i)} \xi^{(i)}. \quad (\text{A9})$$

Appendix B: Inverse-length approximation of the pseudopotential

In this appendix we present the detailed steps to arrive at the inverse-length approximation of the pseudopotential \tilde{U}_{eff} in (37), starting from the pseudopotential U_{eff} in (36). For the convenience of the reader, we import U_{eff} in (36):

$$U_{\text{eff}} = \frac{2}{\rho} + \frac{1}{2r} + 3ax^2 + ay^2 - 2az^2 + \frac{3qx\xi\Delta + qy\eta\Delta - 2qz\zeta\Delta}{\Delta}. \quad (\text{B1})$$

Since the goal is to keep terms up to first order in $1/\text{length}$, all we need to do is to expand the last term in (B1). Denoting the numerator of this term by N and the denominator of this term by D , we see that, together with (24), (25), and (35), $N \in O(\text{length}^2)$ and $D \in O(1)$, as $\text{length} \rightarrow +\infty$. This means, (i) since D is of the order of a constant in length , N should be expanded up to $1/\text{length}$ and (ii) since N is of the order of length^2 , D must be expanded up to $1/\text{length}^3$. This is so, because

$$\begin{aligned} \frac{N}{D} &= \frac{a_2 + a_1 + a_0 + a_{-1} + O(\text{length}^{-2})}{b_0 + b_{-1} + b_{-2} + b_{-3} + O(\text{length}^{-4})} \\ &\approx \frac{1}{b_0} [a_2 + a_1 + a_0 + a_{-1} + O(\text{length}^{-2})] \\ &\times \left\{ 1 - \frac{1}{b_0} [b_{-1} + b_{-2} + b_{-3} + O(\text{length}^{-4})] \right\}^{-1}, \end{aligned} \quad (\text{B2})$$

where a_ν and b_μ denote the terms that scale like length^ν and length^μ of N and D , respectively.

Direct evaluation of a_ν and b_μ for $\nu = 2, 1, 0, -1$ and $\mu = 0, -1, -2, -3$ results in

$$\begin{aligned}
a_1 &= a_0 = b_{-1} = b_{-2} = 0, \\
a_2 &= 36q^2x^2(8-2a)(8+4a) + 4q^2y^2(8+4a)(24-6a) + 16q^2z^2(24-6a)(8-2a), \\
b_0 &= (8-2a)(8+4a)(24-6a), \\
a_{-1} &= 3qx \left\{ 12qx \left[(8-2a) \left(\frac{1}{2r^3} + \frac{2}{\rho^3} - \frac{6z^2}{\rho^5} - \frac{3z^2}{2r^5} \right) \right. \right. \\
&\quad \left. \left. + (8+4a) \left(\frac{1}{2r^3} + \frac{2}{\rho^3} - \frac{6y^2}{\rho^5} - \frac{3y^2}{2r^5} \right) \right] \right. \\
&\quad \left. + 4qy \left[(8+4a) \left(\frac{54xy}{\rho^5} \right) \right] - 8qz \left[(8-2a) \left(\frac{54xz}{\rho^5} \right) \right] \right\} \\
&\quad + qy \left\{ 4qy \left[(8+4a) \left(\frac{18}{\rho^3} - \frac{486x^2}{\rho^5} \right) + (24-6a) \left(\frac{1}{2r^3} + \frac{2}{\rho^3} - \frac{6z^2}{\rho^5} - \frac{3z^2}{2r^5} \right) \right] \right. \\
&\quad \left. + 12qx \left[(8+4a) \left(\frac{54xy}{\rho^5} \right) \right] - 8qz \left[(24-6a) \left(\frac{6yz}{\rho^5} + \frac{3yz}{2r^5} \right) \right] \right\} \\
&\quad - 2qz \left\{ -8qz \left[(24-6a) \left(\frac{1}{2r^3} + \frac{2}{\rho^3} - \frac{6y^2}{\rho^5} - \frac{3y^2}{2r^5} \right) + (8-2a) \left(\frac{18}{\rho^3} - \frac{486x^2}{\rho^5} \right) \right] \right. \\
&\quad \left. + 12qx \left[(8-2a) \left(\frac{54xz}{\rho^5} \right) \right] + 4qy \left[(24-6a) \left(\frac{6yz}{\rho^5} + \frac{3yz}{2r^5} \right) \right] \right\}, \\
b_{-3} &= (8-2a)(8+4a) \left(-\frac{486x^2}{\rho^5} + \frac{18}{\rho^3} \right) \\
&\quad + (8-2a)(24-6a) \left(-\frac{3z^2}{2r^5} + \frac{1}{2r^3} - \frac{6z^2}{\rho^5} + \frac{2}{\rho^3} \right) \\
&\quad + (8+4a)(24-6a) \left(-\frac{3y^2}{2r^5} + \frac{1}{2r^3} - \frac{6y^2}{\rho^5} + \frac{2}{\rho^3} \right). \tag{B3}
\end{aligned}$$

Keeping terms up to 1/length in (B2), together with the results shown in (B3), we obtain

$$\frac{N}{D} \approx \frac{a_2 + a_{-1}}{b_0} - \frac{a_2 b_{-3}}{b_0^2}, \tag{B4}$$

which can be inserted in place of the last term in (B1) to result in the improved pseudopotential \tilde{U}_{eff} in (37).

Appendix C: Analytical prediction of the thee-particle pop-out \leftrightarrow tilt boundary

In this appendix we fill in the steps in the calculation of the explicit solution of x for determining the pop-out \leftrightarrow tilt boundary. We start with (70), where, for fixed a and q , the coefficients δ , β , γ , and z are constants. Introducing the variable ψ to denote x^2 , and

squaring both sides of (70), we obtain

$$\delta^2(9\psi + z^2)^5 = (\beta\psi + \gamma)^2, \quad (\text{C1})$$

which is a quintic equation in ψ . A general formula that yields the solutions of the quintic equation does not exist [42]. However, we note that, together with the transformation

$$9\psi + z^2 \rightarrow \varphi, \quad (\text{C2})$$

we may write

$$\delta^2\varphi^5 - \frac{\beta^2\varphi^2}{81} + \frac{2}{9}\left(\frac{\beta z^2}{9} - \gamma\right)\beta\varphi - \left(\frac{\beta z^2}{9} - \gamma\right)^2 = 0, \quad (\text{C3})$$

which is known as the principal quintic form. By rescaling φ according to

$$\bar{\varphi} = -\frac{2\beta}{9} \frac{1}{\beta z^2/9 - \gamma} \varphi, \quad (\text{C4})$$

we obtain

$$A\bar{\varphi}^5 + B\bar{\varphi}^2 + \bar{\varphi} + 1 = 0, \quad (\text{C5})$$

where

$$A = \left(\frac{9}{2\beta}\right)^5 \delta^2 \left(\frac{\beta z^2}{9} - \gamma\right)^3, \quad B = \frac{1}{4}. \quad (\text{C6})$$

Now, together with z in (69) and δ , β , and γ in (70), we may numerically evaluate the coefficient A in (C6) explicitly as a function of the trap control parameters a and q . We find that, throughout the entire stability region, $|A| \sim 10^{-8} \ll 1$. This means that we may approximate the quintic term in (C5) as 0 and solve the resulting quadratic equation, an excellent approximation if the solution $\bar{\varphi}_0$ of the quadratic equation is such that $|A|\bar{\varphi}_0 \ll 1$. It can straightforwardly be shown that $\bar{\varphi}_0 = -2$, and thus the approximation is indeed excellent. As a result, we obtain

$$x = \sqrt{-\frac{\gamma}{\beta}}. \quad (\text{C7})$$

-
- [1] L. Allen and J. H. Eberly, *Optical Resonance and Two-Level Atoms* (Dover Publications, New York, 1987).
- [2] M. Sargent, M. O. Scully, W. E. Lamb, *Laser Physics* (Addison-Wesley, Reading, MA, 1974).
- [3] J. E. Bayfield and P. M. Koch, Phys. Rev. Lett. **33**, 258 (1974);

- [4] P. M. Koch and K. A. H. van Leeuwen, *Phys. Rep.* **255**, 289 (1995).
- [5] R. Blümel and U. Smilansky, *Physica Scripta* **35**, 15 (1987).
- [6] R. Blümel, A. Buchleitner, R. Graham, L. Sirko, U. Smilansky, and H. Walther, *Phys. Rev. A* **44**, 4521 (1991).
- [7] R. Blümel, S. Fishman, and U. Smilansky, *J. Chem. Phys.* **84**, 2604 (1986).
- [8] W. Paul, *Rev. Mod. Phys.* **62**, 531 (1990).
- [9] P. K. Ghosh, *Ion Traps* (Clarendon Press, Oxford, 1995).
- [10] R. Blümel, J. M. Chen, E. Peik, W. Quint, W. Schleich, Y. R. Shen, and H. Walther, *Nature* **334**, 309 (1988).
- [11] A. G. Fainshtein, N. L. Manakov, and L. P. Rapoport, *J. Phys. B: Atom. Molec. Phys.* **11**, 2561 (1978).
- [12] *Atomic, Molecular, and Optical Physics Handbook*, edited by G. W. F. Drake (American Institute of Physics, Woodbury, New York, 1996).
- [13] G. Floquet, *Annales de l'cole Normale Suprieure* **12**, 47 (1883).
- [14] *Handbook of Mathematical Functions*, edited by M. Abramowitz and I. A. Stegun (National Bureau of Standards, Gaithersburg, MD, 1964).
- [15] H.-J. Stöckmann, *Quantum Chaos: An Introduction* (Cambridge University Press, New York, 1999).
- [16] R. Blümel and W. P. Reinhardt, *Chaos in Atomic Physics* (Cambridge University Press, Cambridge, 1997).
- [17] X. Chu and Shih-I Chu, *Phys. Rev. A* **63**, 013414 (2000).
- [18] M. Combescure, *J. Stat. Phys.* **59**, 679 (1990).
- [19] L. D. Landau and E. M. Lifshits, *Mechanics*, second edition (Pergamon Press, Oxford, 1976).
- [20] M. G. Moore and R. Blümel, *Phys. Rev. A* **50**, R4453 (1994).
- [21] J. A. Hoffnagle and R. G. Brewer, *Appl. Phys. B* **60**, 113 (1995).
- [22] M. G. Moore and R. Blümel, *Physica Scripta* **T59**, 429 (1995).
- [23] R. Blatt and G. Werth, *Phys. Rev. A* **25**, 1476 (1982).
- [24] R. F. Wuerker, H. Shelton, and R. V. Langmuir, *J. Appl. Phys.* **30**, 342 (1959).
- [25] F. Diedrich, E. Peik, J. M. Chen, W. Quint, and H. Walther, *Phys. Rev. Lett.* **59**, 2931 (1987).
- [26] D. J. Wineland, J. C. Bergquist, W. M. Itano, J. J. Bollinger, and C. H. Manney, *Phys. Rev. Lett.* **59**, 2935 (1987).

- [27] F. Diedrich, J. C. Bergquist, W. M. Itano, and D. J. Wineland, *Phys. Rev. Lett.* **62**, 403 (1989).
- [28] Y. S. Nam, E. B. Jones, and R. Blümel, *Phys. Rev. A* **90**, 013402 (2014).
- [29] R. Blümel, C. Kappler, W. Quint, and H. Walther, *Phys. Rev. A* **40**, 808 (1989).
- [30] W. H. Press, S. A. Teukolsky, W. T. Vetterling, and B. P. Flannery, *Numerical Recipes*, second edition (Cambridge University Press, Cambridge, 1992).
- [31] H. Walther, *Advances in Atomic, Molecular, and Optical Physics* **31**, 137 (1993).
- [32] J. D. Tarnas, Y. S. Nam, and R. Blümel, *Phys. Rev. A* **88**, 041401 (2013).
- [33] S. T. Thornton and J. B. Marion, *Classical Dynamics of Particles and Systems*, (Brooks/Cole, Belmont, CA, 2004).
- [34] J. W. Emmert, M. Moore, and R. Blümel, *Phys. Rev. A* **48**, R1757 (1993).
- [35] I. S. Gradshteyn and I. M. Ryzhik, *Table of Integrals, Series, and Products*, fifth edition, A. Jeffrey, editor (Academic Press, Boston, 1994), ¶14.314, p. 1145.
- [36] L. Föppl, *J. reine angew. Math.* **141**, 251 (1912).
- [37] *Quantum Dots - Optics, Electron Transport and Future Applications*, edited by A. Tartakovskii (Cambridge University Press, Cambridge, 2012).
- [38] M. A. Kastner, *Physics Today* **46** (1), 24 (1993).
- [39] A. J. Lichtenberg and M. A. Lieberman, *Regular and Stochastic Motion*, Vol. **38** of Applied Mathematical Sciences (Springer, New York, 1983).
- [40] H. Friedrich, *Theoretical Atomic Physics*, third edition (Springer, Berlin, 2006).
- [41] D. C. Lay, *Linear Algebra and its Applications* (Addison-Wesley, New York, 2003).
- [42] N. Jacobson, *Basic Algebra I* (Dover, Mineola, NY, 2009).